Eur. Phys. J. C (2012) 72:1970
DOI 10.1140/epjc/s10052-012-1970-9

THE EUROPEAN PHYSICAL JOURNAL C

Regular Article - Experimental Physics

Measurement of dijet production in diffractive deep-inelastic scattering with a leading proton at HERA

The H1 Collaboration

F.D. Aaron[6,n,w], **C. Alexa**[6,n], **V. Andreev**[26,f], **S. Backovic**[31,o], **A. Baghdasaryan**[40], **S. Baghdasaryan**[40], **E. Barrelet**[30], **W. Bartel**[12], **K. Begzsuren**[37], **A. Belousov**[26,f], **P. Belov**[12], **J.C. Bizot**[28], **V. Boudry**[29], **I. Bozovic-Jelisavcic**[2], **J. Bracinik**[3,c], **G. Brandt**[12], **M. Brinkmann**[12], **V. Brisson**[28], **D. Britzger**[12], **D. Bruncko**[17,g], **A. Bunyatyan**[14,40], **G. Buschhorn**[27,†], **L. Bystritskaya**[25,l], **A.J. Campbell**[12], **K.B. Cantun Avila**[23,k], **F. Ceccopieri**[4,5,d], **K. Cerny**[33,i], **V. Cerny**[17,g,v], **V. Chekelian**[27], **J.G. Contreras**[23,k], **J.A. Coughlan**[7,c], **J. Cvach**[32,i], **J.B. Dainton**[19,c], **K. Daum**[39,a,r], **B. Delcourt**[28], **J. Delvax**[4,5,d], **E.A. De Wolf**[4,5,d], **C. Diaconu**[22], **M. Dobre**[13,b,y,z], **V. Dodonov**[14], **A. Dossanov**[27], **A. Dubak**[31,o,u], **G. Eckerlin**[12], **S. Egli**[38], **A. Eliseev**[26,f], **E. Elsen**[12], **L. Favart**[4,5,d], **A. Fedotov**[25,l], **R. Felst**[12], **J. Feltesse**[11], **J. Ferencei**[17,g], **D.-J. Fischer**[12], **M. Fleischer**[12], **A. Fomenko**[26,f], **E. Gabathuler**[19,c], **J. Gayler**[12], **S. Ghazaryan**[12], **A. Glazov**[12], **L. Goerlich**[8,e], **N. Gogitidze**[26,f], **M. Gouzevitch**[12,t], **C. Grab**[42,j], **A. Grebenyuk**[12], **T. Greenshaw**[19,c], **B.R. Grell**[12], **G. Grindhammer**[27], **S. Habib**[12], **D. Haidt**[12], **C. Helebrant**[12], **R.C.W. Henderson**[18,c], **E. Hennekemper**[16,b], **H. Henschel**[41], **M. Herbst**[16,b], **G. Herrera**[24,k], **M. Hildebrandt**[38], **K.H. Hiller**[41], **D. Hoffmann**[22], **R. Horisberger**[38], **T. Hreus**[4,5,d,s], **F. Huber**[15,b], **M. Jacquet**[28], **X. Janssen**[4,5,d], **L. Jönsson**[21,h], **H. Jung**[12,4,5,d,aa], **M. Kapichine**[10], **I.R. Kenyon**[3,c], **C. Kiesling**[27], **M. Klein**[19,c], **C. Kleinwort**[12], **T. Kluge**[19,c], **R. Kogler**[12], **P. Kostka**[41], **M. Kraemer**[12], **J. Kretzschmar**[19,c], **K. Krüger**[16,b], **M.P.J. Landon**[20,c], **W. Lange**[41], **G. Laštovička-Medin**[31,o], **P. Laycock**[19,c], **A. Lebedev**[26,f], **V. Lendermann**[16,b], **S. Levonian**[12], **K. Lipka**[12,y], **B. List**[12], **J. List**[12], **R. Lopez-Fernandez**[24,k], **V. Lubimov**[25,l], **A. Makankine**[10], **E. Malinovski**[26,f], **P. Marage**[4,5,d], **H.-U. Martyn**[1], **S.J. Maxfield**[19,c], **A. Mehta**[19,c], **A.B. Meyer**[12], **H. Meyer**[39], **J. Meyer**[12], **S. Mikocki**[8,e], **I. Milcewicz-Mika**[8,e], **F. Moreau**[29], **A. Morozov**[10], **J.V. Morris**[7,c], **M. Mudrinic**[2], **K. Müller**[43,j], **Th. Naumann**[41], **P.R. Newman**[3,c], **C. Niebuhr**[12], **D. Nikitin**[10], **G. Nowak**[8,e], **K. Nowak**[12], **J.E. Olsson**[12], **D. Ozerov**[25,l], **P. Pahl**[12], **V. Palichik**[10], **I. Panagoulias**[12,m,p], **M. Pandurovic**[2], **Th. Papadopoulou**[12,m,p], **C. Pascaud**[28], **G.D. Patel**[19,c], **E. Perez**[11,t], **A. Petrukhin**[12], **I. Picuric**[31,o], **S. Piec**[12], **H. Pirumov**[15,b], **D. Pitzl**[12], **R. Plačakytė**[13,b], **B. Pokorny**[33,i], **R. Polifka**[33,i,ab], **B. Povh**[14], **V. Radescu**[15,b], **N. Raicevic**[31,o], **T. Ravdandorj**[37], **P. Reimer**[32,i], **E. Rizvi**[20,c], **P. Robmann**[43,j], **R. Roosen**[4,5,d], **A. Rostovtsev**[25,l], **M. Rotaru**[6,n], **J.E. Ruiz Tabasco**[23,k], **S. Rusakov**[26,f], **D. Šálek**[33,i], **D.P.C. Sankey**[7,c], **M. Sauter**[15,b], **E. Sauvan**[22], **S. Schmitt**[12], **L. Schoeffel**[11], **A. Schöning**[15,b], **H.-C. Schultz-Coulon**[16,b], **F. Sefkow**[12], **L.N. Shtarkov**[26,f], **S. Shushkevich**[12], **T. Sloan**[18,c], **I. Smiljanic**[2], **Y. Soloviev**[26,f], **P. Sopicki**[8,e], **D. South**[12], **V. Spaskov**[10], **A. Specka**[29], **Z. Staykova**[4,5,d], **M. Steder**[12], **B. Stella**[34,35], **G. Stoicea**[6,n], **U. Straumann**[43,j], **T. Sykora**[4,5,33,i], **P.D. Thompson**[3,c], **T.H. Tran**[28], **D. Traynor**[20,c], **P. Truöl**[43,j], **I. Tsakov**[36,f], **B. Tseepeldorj**[37,x], **J. Turnau**[8,e], **A. Valkárová**[33,i], **C. Vallée**[22], **P. Van Mechelen**[4,5,d], **Y. Vazdik**[26,f], **D. Wegener**[9,b], **E. Wünsch**[12], **J. Žáček**[33,i], **J. Zálešák**[32,i], **Z. Zhang**[28], **A. Zhokin**[25,l], **H. Zohrabyan**[40], **F. Zomer**[28]

[1] I. Physikalisches Institut der RWTH, Aachen, Germany
[2] Vinca Institute of Nuclear Sciences, University of Belgrade, 1100 Belgrade, Serbia
[3] School of Physics and Astronomy, University of Birmingham, Birmingham, UK
[4] Inter-University Institute for High Energies ULB-VUB, Brussels, Belgium
[5] Universiteit Antwerpen, Antwerpen, Belgium
[6] National Institute for Physics and Nuclear Engineering (NIPNE), Bucharest, Romania
[7] Rutherford Appleton Laboratory, Chilton, Didcot, UK
[8] Institute for Nuclear Physics, Cracow, Poland
[9] Institut für Physik, TU Dortmund, Dortmund, Germany
[10] Joint Institute for Nuclear Research, Dubna, Russia
[11] CEA, DSM/Irfu, CE-Saclay, Gif-sur-Yvette, France
[12] DESY, Hamburg, Germany
[13] Institut für Experimentalphysik, Universität Hamburg, Hamburg, Germany
[14] Max-Planck-Institut für Kernphysik, Heidelberg, Germany
[15] Physikalisches Institut, Universität Heidelberg, Heidelberg, Germany

[16]Kirchhoff-Institut für Physik, Universität Heidelberg, Heidelberg, Germany
[17]Institute of Experimental Physics, Slovak Academy of Sciences, Košice, Slovak Republic
[18]Department of Physics, University of Lancaster, Lancaster, UK
[19]Department of Physics, University of Liverpool, Liverpool, UK
[20]Queen Mary and Westfield College, London, UK
[21]Physics Department, University of Lund, Lund, Sweden
[22]CPPM, Aix-Marseille Univ., CNRS/IN2P3, 13288 Marseille, France
[23]Departamento de Fisica Aplicada, CINVESTAV, Mérida, Yucatán, México
[24]Departamento de Fisica, CINVESTAV IPN, México City, México
[25]Institute for Theoretical and Experimental Physics, Moscow, Russia
[26]Lebedev Physical Institute, Moscow, Russia
[27]Max-Planck-Institut für Physik, Munich, Germany
[28]LAL, Université Paris-Sud, CNRS/IN2P3, Orsay, France
[29]LLR, Ecole Polytechnique, CNRS/IN2P3, Palaiseau, France
[30]LPNHE, Université Pierre et Marie Curie Paris 6, Université Denis Diderot Paris 7, CNRS/IN2P3, Paris, France
[31]Faculty of Science, University of Montenegro, Podgorica, Montenegro
[32]Institute of Physics, Academy of Sciences of the Czech Republic, Prague, Czech Republic
[33]Faculty of Mathematics and Physics, Charles University, Prague, Czech Republic
[34]Dipartimento di Fisica, Università di Roma Tre, Rome, Italy
[35]INFN Roma 3, Rome, Italy
[36]Institute for Nuclear Research and Nuclear Energy, Sofia, Bulgaria
[37]Institute of Physics and Technology of the Mongolian Academy of Sciences, Ulaanbaatar, Mongolia
[38]Paul Scherrer Institut, Villigen, Switzerland
[39]Fachbereich C, Universität Wuppertal, Wuppertal, Germany
[40]Yerevan Physics Institute, Yerevan, Armenia
[41]DESY, Zeuthen, Germany
[42]Institut für Teilchenphysik, ETH, Zürich, Switzerland
[43]Physik-Institut der Universität Zürich, Zürich, Switzerland

Received: 2 November 2011 / Revised: 2 March 2012 / Published online: 18 April 2012

[a] e-mail: daum@mail.desy.de

[b]Supported by the Bundesministerium für Bildung und Forschung, FRG, under contract numbers 05H09GUF, 05H09VHC, 05H09VHF, 05H16PEA.

[c]Supported by the UK Science and Technology Facilities Council, and formerly by the UK Particle Physics and Astronomy Research Council.

[d]Supported by FNRS-FWO-Vlaanderen, IISN-IIKW and IWT and by Interuniversity Attraction Poles Programme, Belgian Science Policy.

[e]Partially Supported by Polish Ministry of Science and Higher Education, grant DPN/N168/DESY/2009.

[f]Supported by the Deutsche Forschungsgemeinschaft.

[g]Supported by VEGA SR grant no. 2/7062/27.

[h]Supported by the Swedish Natural Science Research Council.

[i]Supported by the Ministry of Education of the Czech Republic under the projects LC527, INGO-LA09042 and MSM0021620859.

[j]Supported by the Swiss National Science Foundation.

[k]Supported by CONACYT, México, grant 48778-F.

[l]Russian Foundation for Basic Research (RFBR), grant no 1329.2008.2 and Rosatom.

[m]This project is co-funded by the European Social Fund (75 %) and National Resources (25 %)—(EPEAEK II)—PYTHAGORAS II.

[n]Supported by the Romanian National Authority for Scientific Research under the contract PN 09370101.

[o]Partially Supported by Ministry of Science of Montenegro, no. 05-1/3-3352.

[p]Also at Physics Department, National Technical University, Zografou Campus, GR-15773 Athens, Greece.

[r]Also at Rechenzentrum, Universität Wuppertal, Wuppertal, Germany.

[s]Also at University of P.J. Šafárik, Košice, Slovak Republic.

[t]Also at CERN, Geneva, Switzerland.

[u]Also at Max-Planck-Institut für Physik, Munich, Germany.

[v]Also at Comenius University, Bratislava, Slovak Republic.

[w]Also at Faculty of Physics, University of Bucharest, Bucharest, Romania.

[x]Also at Ulaanbaatar University, Ulaanbaatar, Mongolia.

[y]Supported by the Initiative and Networking Fund of the Helmholtz Association (HGF) under the contract VH-NG-401.

[z]Absent on leave from NIPNE-HH, Bucharest, Romania.

[aa]On leave of absence at CERN, Geneva, Switzerland.

[ab]Also at Department of Physics, University of Toronto, Toronto, Ontario, Canada M5S 1A7.

[†]Deceased.

Abstract The cross section of diffractive deep-inelastic scattering $ep \to eXp$ is measured, where the system X contains at least two jets and the leading final state proton is detected in the H1 Forward Proton Spectrometer. The measurement is performed for fractional proton longitudinal momentum loss $x_{\mathbb{P}} < 0.1$ and covers the range $0.1 < |t| < 0.7\ \mathrm{GeV}^2$ in squared four-momentum transfer at the proton vertex and $4 < Q^2 < 110\ \mathrm{GeV}^2$ in photon virtuality. The differential cross sections extrapolated to $|t| < 1\ \mathrm{GeV}^2$ are in agreement with next-to-leading order QCD predictions based on diffractive parton distribution functions extracted from measurements of inclusive and dijet cross sections in diffractive deep-inelastic scattering. The data are also compared with leading order Monte Carlo models.

1 Introduction

Diffractive processes such as $ep \to eXY$, where the systems X and Y are separated in rapidity, have been studied extensively in deep-inelastic scattering (DIS) at the electron[1]-proton collider HERA [1–8]. Diffractive DIS events can be viewed as resulting from processes in which the photon probes a net colour singlet combination of exchanged partons. The photon virtuality Q^2, the high transverse momentum of jets or a heavy quark mass can provide a hard scale for perturbative QCD calculations. For semi-inclusive DIS processes such as $ep \to eXp'$ the hard scattering QCD collinear factorisation theorem [9] allows the definition of diffractive parton distribution functions (DPDFs). The dependence of diffractive DIS on a hard scale can thus be treated in a manner similar to the treatment of inclusive DIS, for example through the application of the DGLAP parton evolution equations [10–14]. DPDFs have been determined from QCD fits to diffractive DIS measurements at HERA [2, 3, 8]. The inclusive diffractive DIS cross section is directly proportional to the sum of the quark DPDFs and constrains the gluon DPDF via scaling violations. The production of diffractive hadronic final states containing heavy quarks or jets proceeds mainly via boson gluon fusion (BGF) and therefore directly constrains the diffractive gluon density [3, 8].

In previous analyses at HERA, diffractive DIS events have been selected on the basis of the presence of a large rapidity gap (LRG) between system Y, which consists of the outgoing proton or its dissociative excitations, and the hadronic final state, system X [3, 4]. The main advantage of the LRG method is its high acceptance for diffractive processes. A complementary way to study diffraction is by direct measurement of the outgoing proton, which remains intact in elastic interactions. This is achieved by the H1 experiment using the Forward Proton Spectrometer (FPS) [15, 16], which is a set of tracking detectors along the proton beam line. Despite the low geometrical acceptance of the FPS, this method of selecting diffractive events has several advantages. The squared four-momentum transfer at the proton vertex, t, can be reconstructed with the FPS, while this is only possible in exclusive final states in the LRG case. The FPS method selects events in which the proton scatters elastically, whereas the LRG method does not distinguish between the case where the scattered proton remains intact or where it dissociates into a system of low mass M_Y. The FPS method also allows measurements to be performed at higher values of fractional proton longitudinal momentum loss, $x_{\mathbb{P}}$, than possible using the LRG method.

This paper presents the first measurement of the cross section for the diffractive DIS process $ep \to ejjX'p$, with two jets and a leading proton in the final state. The diffractive dijet cross sections are compared with next-to-leading order (NLO) QCD predictions based on DPDFs from H1 [2, 3] and with leading order (LO) Monte Carlo (MC) simulations based on different models.

The dijet cross sections are measured for two event topologies: for a topology where two jets are found in the central pseudorapidity range, labelled as 'two central jets', and for a topology where one jet is central and one jet is more forward[2], labelled as 'one central + one forward jet'. The universality of DPDFs is studied using events with two central jets. The distributions of the proton vertex variables $x_{\mathbb{P}}$ and t are compared to those of the inclusive diffractive DIS case. This comparison tests the proton vertex factorisation hypothesis which assumes that the DIS variable factorise from the four-momentum of the final state proton. The data are also compared directly with the LRG measurement of the dijet cross section in diffractive DIS [3] in order to test the compatibility of the two experimental techniques. Finally, events with one central and one forward jet are used to investigate diffractive DIS in a region of phase space where effects beyond DGLAP parton evolution may be enhanced. This topology is not accessible with the LRG method since the rapidity gap requirement limits the pseudorapidity of the reconstructed jets to the central region.

2 Kinematics

Figure 1 illustrates the dominant process for diffractive dijet production in DIS. The incoming electron with four-momentum k interacts with the proton with four-momentum P via the exchange of a virtual photon with four-momentum q. The DIS kinematic variables are defined as:

[1] In this paper "electron" is used to denote both electron and positron unless otherwise stated.

[2] The forward direction is defined by the proton beam direction.

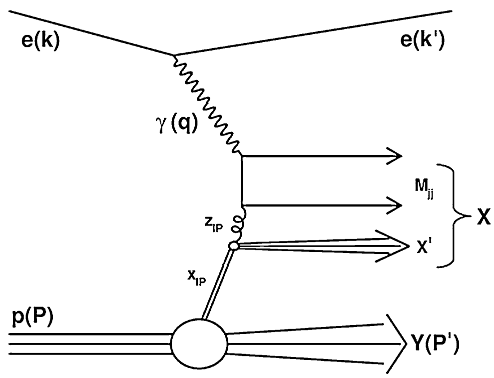

Fig. 1 The leading order boson gluon fusion diagram for dijet production in diffractive DIS

$$Q^2 = -q^2 = (k - k')^2,$$
$$x = \frac{-q^2}{2P \cdot q}, \qquad y = \frac{P \cdot q}{P \cdot k}, \tag{1}$$

where Q^2 is the photon virtuality, x is the longitudinal momentum fraction of the proton carried by the struck quark and y is the inelasticity of the process. These three variables are related via $Q^2 = xys$, where s denotes the ep centre-of-mass energy squared.

The hadronic final state of diffractive events consists of two systems X and Y, separated by a gap in rapidity. In general, the system Y is the outgoing proton or one of its low mass excitations. In events where the outgoing proton remains intact, $M_Y = m_p$, the mass of the proton. The kinematics of diffractive DIS are described by:

$$x_{\mathbb{P}} = \frac{q \cdot (P - P')}{q \cdot P}, \quad t = (P' - P)^2,$$
$$\beta = \frac{-q^2}{2q \cdot (P - P')} = \frac{x}{x_{\mathbb{P}}}, \tag{2}$$

where $x_{\mathbb{P}}$ denotes the longitudinal momentum fraction of the proton carried by the colour singlet exchange, t is the squared four-momentum transfer at the proton vertex and β is the fractional momentum of the diffractive exchange carried by the struck parton. The longitudinal momentum fraction of the diffractive exchange carried by the parton entering the hard scatter is

$$z_{\mathbb{P}} = \frac{q \cdot v}{q \cdot (P - P')}, \tag{3}$$

where v is the four-momentum of the parton.

3 Theoretical framework and Monte Carlo models

Within Regge phenomenology, cross sections at high energies are described by the exchange of Regge trajectories. The diffractive cross section is dominated by a trajectory usually called the Pomeron ($\mathbb{P}$). In analyses of HERA data [2, 3, 8], diffractive DIS cross sections are interpreted assuming 'proton vertex factorisation' which provides a description of diffractive DIS in terms of a resolved Pomeron [17, 18]. The QCD factorisation theorem and DGLAP parton evolution equations are applied to the dependence of the cross section on Q^2 and β, while a Regge inspired approach is used to express the dependence on $x_{\mathbb{P}}$ and t.

The resolved Pomeron (RP) model [17] is implemented in the RAPGAP event generator [19]. RAPGAP implements both a leading Pomeron ($\mathbb{P}$) trajectory and a sub-leading 'Reggeon' ($\mathbb{R}$). In this analysis the DPDF H1 2006 Fit B [2] is used, which employs the Owens pion PDFs [20] for the partonic content of the Reggeon. The Reggeon contribution is significant for $x_{\mathbb{P}} > 0.01$. Higher order QCD radiation is modelled by parton showers. Processes with a resolved virtual photon are also included, with the photon structure function given by the SaS-G 2D LO parameterisation [21].

In the two-gluon Pomeron (TGP) model [22, 23], the diffractive exchange is modelled at LO as the interaction of a colourless pair of gluons with a $q\bar{q}$ or $q\bar{q}g$ configuration emerging from the photon. The model is implemented in the RAPGAP generator. Higher order effects are simulated using parton showers. The unintegrated gluon PDF of set A0 [24] is used.

In the soft colour interaction (SCI) model [25, 26], the diffractive exchange is modelled via non-diffractive DIS scattering with subsequent colour rearrangement between the partons in the final state, which can produce a colour singlet system separated by a large gap in pseudorapidity. A refined version of the SCI model which uses a generalised area law (GAL) for the probability of having a soft colour interaction [27] is used in this analysis (SCI+GAL). Predictions for diffractive dijet production within the SCI+GAL model are obtained using the leading order generator program LEPTO [28]. Higher order effects are simulated using parton showers [29, 30]. The calculations are based on the CTEQ6L [31] proton PDFs. The probability for a soft colour interaction, R, has been tuned to 0.3 to describe the total diffractive dijet cross section as measured using the 'two central jets' topology.

In all three models hadronisation is simulated using the Lund string model [32] implemented within the PYTHIA program [33, 34].

In this analysis the dijet cross section is also compared to NLO QCD calculations. Assuming proton vertex factorisation, NLO QCD predictions for the diffractive partonic dijet cross section are calculated in bins of $x_{\mathbb{P}}$ using the NLOJET++ [35] program and integrated over the full $x_{\mathbb{P}}$ range of the measurement. The renormalisation and factorisation scales are set to $\mu_r = \mu_f = \sqrt{Q^2 + \langle P_T^* \rangle^2}$, where $\langle P_T^* \rangle$ is the mean of the transverse momenta of the two leading jets in the hadronic centre-of-mass frame. In order to estimate the uncertainties of the NLO QCD calculations due to missing higher orders, the factorisation scale μ_f and renormalisation scale μ_r are varied simultaneously by factors of 0.5 and 2. The average uncertainty arising from the variation of the scale is about 33 %. The DPDFs used in the NLO QCD calculations are H1 2006 Fit B [2] and H1 2007 Jets [3]. The H1 2007 Jets fit is based on the diffractive inclusive and dijet data while H1 2006 Fit B is based on inclusive diffractive data only. The uncertainty of the NLO QCD calculations due to DPDFs is estimated by propagating the DPDF errors. The DPDF errors are available only for the DPDF set H1 2006 Fit B. The average uncertainty resulting from the DPDF errors is about 7 % which is much smaller than the scale uncertainty. In the NLOJET++ calculations the strong coupling is set via $\Lambda^{(4)}_{\overline{\rm MS}} = 340 \pm 37$ MeV for four flavours, which corresponds to the value of $\alpha_s^{(5)}(M_Z) = 0.119 \pm 0.002$ for five flavours in the 2-loop approximation [36, 37]. The average uncertainty resulting from the variation of $\alpha_s(M_Z)$ is about 1.5 %. In order to demonstrate the size of the NLO corrections, the QCD calculations are also performed at leading order.

The NLO QCD partonic cross sections are corrected to the level of stable hadrons by evaluating effects due to initial and final state parton showering, fragmentation and hadronisation. The hadronisation corrections are defined in each bin as a ratio of the cross section obtained at the level of stable hadrons to the partonic cross sections. Two sets of hadronisation corrections have been obtained using the RAPGAP generator using two different parton shower models: parton showers based on leading logarithm DGLAP splitting functions in leading order α_s [10–13] and parton showers based on the colour dipole model as implemented in ARIADNE [38]. The nominal set of corrections $(1+\delta_{\rm had})$ is taken as the average of the two sets, while the difference between them is considered as the hadronisation uncertainty. The average hadronisation corrections are of about 0.9 with an estimated uncertainty of about 7 %. Uncertainties of the NLO QCD predictions arising due to scale variations and hadronisation corrections are added in quadrature.

In order to compare with the results of the FPS measurements, NLO QCD predictions as well as predictions of the RP model are scaled down by a factor of 1.20 [16] due to the fact that the DPDF sets H1 2006 Fit B and H1 2007 Jets use LRG data which contain a proton dissociation contribution. The t-dependence of the $\mathbb{P}$ and $\mathbb{R}$ fluxes implemented in the H1 DPDF sets and the RP model are tuned to reproduce the t-dependence measured in inclusive diffractive DIS with a leading proton in the final state [15].

4 Experimental technique

The $e^{\pm}p$ data used in this analysis were collected with the H1 detector in the years 2005 to 2007 and correspond to an integrated luminosity of 156.6 pb^{-1}. During this period the HERA collider was operated at electron and proton beam energies of $E_e = 27.6$ GeV and $E_p = 920$ GeV respectively, corresponding to an ep centre-of-mass energy of $\sqrt{s} = 319$ GeV.

4.1 H1 detector

A detailed description of the H1 detector can be found elsewhere [39–41]. Here, the components most relevant for the presented measurement are described briefly. A right-handed coordinate system is employed with the origin at the nominal interaction point, where the z-axis pointing in the proton beam or forward direction and the $x(y)$ axis points in the horizontal (vertical) direction. The polar angle θ is measured with respect to the proton beam axis and the pseudorapidity is defined as $\eta = -\ln\tan(\theta/2)$.

The Central Tracking Detector (CTD), with a polar angle coverage of $20° < \theta < 160°$, is used to reconstruct the interaction vertex and to measure the momenta of charged particles from the curvature of their trajectories in the 1.16 T field provided by a superconducting solenoid. Scattered electrons with polar angles in the range $154° < \theta'_e < 176°$ are measured in a lead/scintillating-fibre calorimeter, the SpaCal [41]. The energy resolution is $\sigma(E)/E \approx 7\ \%/\sqrt{E[\rm GeV]} \oplus 1\ \%$ as determined from the test beam measurement [42, 43]. A Backward Proportional Chamber (BPC) in front of the SpaCal is used to measure the electron polar angle. The finely segmented Liquid Argon (LAr) sampling calorimeter surrounds the tracking system and covers the range in polar angle $4° < \theta < 154°$ corresponding to a pseudorapidity range $-1.5 < \eta < 3.4$. The LAr calorimeter consists of an electromagnetic section with lead as the absorber and a hadronic section with steel as the absorber. The total depth varies with θ between 4.5 and 8 interaction lengths. The energy resolution, determined from test beam measurements [42, 43], is $\sigma(E)/E \approx 11\ \%/\sqrt{E[\rm GeV]} \oplus 1\ \%$ for electrons and $\sigma(E)/E \approx 50\ \%/\sqrt{E[\rm GeV]} \oplus 2\ \%$ for hadrons. The hadronic final state is reconstructed using an energy flow algorithm which combines charged particles measured in the CTD with information from the SpaCal and LAr calorimeters [44].

The luminosity is determined by measuring the rate of the Bethe-Heitler process $ep \to ep\gamma$ detected in a photon detector located at $z = -103$ m.

The energy and scattering angle of the leading proton are obtained from track measurements in the FPS [45]. Protons scattered at small angles are deflected by the proton beam-line magnets into a system of detectors placed within the proton beam pipe inside two movable stations, known as Roman Pots. Both Roman Pot stations contain four planes, where each plane consists of five layers of scintillating fibres, which together measure two orthogonal coordinates in the (x, y) plane. The fibre coordinate planes are sandwiched between planes of scintillator tiles used for the trigger. The stations approach the beam horizontally and are positioned at $z = 61$ m and $z = 80$ m. The detectors are sensitive to scattered protons which lose less than 10 % of their energy in the *ep* interaction and are scattered through angles below 1 mrad.

The energy resolution of the FPS is approximately 5 GeV within the measured range. The absolute energy scale uncertainty is 1 GeV. The effective resolution in the reconstruction of the transverse momentum components of the scattered proton with respect to the incident proton is determined to be ∼50 MeV for P_x and ∼150 MeV for P_y, dominated by the intrinsic transverse momentum spread of the proton beam at the interaction point. The scale uncertainties in the transverse momentum measurements are 10 MeV for P_x and 30 MeV for P_y. Further details of the analysis of the FPS resolution and scale uncertainties can be found elsewhere [16]. For a leading proton which passes through both FPS stations, the track reconstruction efficiency is 48 % on average.

4.2 Kinematic reconstruction

The inclusive DIS variables Q^2, x and the inelasticity y are reconstructed by combining information from the scattered electron and the hadronic final state using the following method [1]:

$$y = y_e^2 + y_d - y_d^2,$$
$$Q^2 = \frac{4E_e^2(1-y)}{\tan^2(\theta'_e/2)}, \qquad x = \frac{Q^2}{sy}. \tag{4}$$

Here, y_e and y_d denote the values of y obtained from the scattered electron only (electron method) and from the angles of the electron and the hadronic final state (double angle method), respectively [46, 47].

The observable $x_{\mathbb{P}}$ is reconstructed as:

$$x_{\mathbb{P}} = 1 - E'_p/E_p, \tag{5}$$

where E'_p is the measured energy of the leading proton in the FPS. The quantity β is reconstructed as $\beta = x/x_{\mathbb{P}}$. The squared four-momentum transfer at the proton vertex is reconstructed using the transverse momentum P_T of the leading proton measured with the FPS and $x_{\mathbb{P}}$ as described above, such that:

$$t = t_{\min} - \frac{P_T^2}{1 - x_{\mathbb{P}}}, \quad t_{\min} = -\frac{x_{\mathbb{P}}^2 m_p^2}{1 - x_{\mathbb{P}}}, \tag{6}$$

where $|t_{\min}|$ is the minimum kinematically accessible value of $|t|$. The absolute resolution in t varies over the measured range from 0.06 GeV^2 at $|t| = 0.1$ GeV^2 to 0.17 GeV^2 at $|t| = 0.7$ GeV^2.

An estimator for the momentum fraction $z_{\mathbb{P}}$ is defined at the level of stable hadrons as:

$$z_{\mathbb{P}} = \frac{Q^2 + M_{jj}^2}{x_{\mathbb{P}} y s}, \tag{7}$$

where M_{jj} denotes the invariant mass of the dijet system. The cross sections are studied in terms of the DIS variables $y, Q^2, \beta, z_{\mathbb{P}}$, the proton vertex variables $x_{\mathbb{P}}$ and t, the jet variables P_T^* and η, and

$$\langle P_T^* \rangle = \frac{1}{2}\left(P_{T,1}^* + P_{T,2}^*\right),$$
$$\left|\Delta\eta^*\right| = \left|\eta_1^* - \eta_2^*\right|, \qquad \left|\Delta\phi^*\right| = \left|\phi_1^* - \phi_2^*\right|, \tag{8}$$

where $P_{T,1}^*, \eta_1^*, \phi_1^*$ and $P_{T,2}^*, \eta_2^*, \phi_2^*$ are transverse momenta, pseudorapidities and azimuthal angles of the axes of the leading and next-to-leading jets, respectively, reconstructed in the hadronic centre-of-mass frame. The indices 1, 2 stand for the two jets used in the specific analyses.

4.3 Event selection

The events used in the 'two central jets' and 'one central + one forward jet' analyses are triggered on the basis of a coincidence of a signal in the FPS trigger scintillator tiles and in the electromagnetic SpaCal. The trigger efficiency, calculated using events collected with independent triggers, is found to be 99 % on average and is independent of kinematic variables.

4.3.1 DIS selection

The selection of DIS events is based on the identification of the scattered electron as the most energetic electromagnetic cluster in the SpaCal calorimeter. The energy E'_e and polar angle θ'_e of the scattered electron are determined from the SpaCal cluster and the interaction vertex reconstructed in the CTD. The electron candidate is required to be in range $154° < \theta'_e < 176°$ and $E'_e > 10$ GeV. In order to improve background rejection, an additional requirement on the transverse cluster radius, estimated using square root energy weighting [48], of less then 4 cm is imposed.

The reconstructed z coordinate of the event vertex is required to be within ±35 cm of the mean position. At least one track originating from the interaction vertex and reconstructed in the CTD is required to have a transverse momentum above 0.1 GeV.

The quantity $\sum(E - P_z)$, summed over the energies and longitudinal momenta of all reconstructed particles including the electron, is required to be between 35 GeV and 70 GeV. For neutral current DIS events this quantity is expected to be twice the electron beam energy when neglecting detector effects and QED radiation. This requirement is applied to remove radiative DIS events and photoproduction background.

In order to ensure a good detector acceptance the measurement is restricted to the ranges $4 < Q^2 < 110\ \mathrm{GeV}^2$ and $0.05 < y < 0.7$.

4.3.2 Leading proton selection

A high FPS acceptance is ensured by requiring the energy of the leading proton E'_p to be greater than 90 % of the proton beam energy E_p and the horizontal and vertical projections of the transverse momentum to be in the ranges $-0.63 < P_x < -0.27$ GeV and $|P_y| < 0.8$ GeV, respectively. Additionally, t is restricted to the range $0.1 < |t| < 0.7\ \mathrm{GeV}^2$.

The quantity $\sum(E + P_z)$, summed over all reconstructed particles including the leading proton, is required to be below 1880 GeV. For neutral current DIS events this quantity is expected to be twice the proton beam energy. This requirement is applied to suppress cases where a DIS event reconstructed in the central detector coincides with background in the FPS, for example due to interactions between off-momentum protons from the beam halo with residual gas within the beampipe.

Previous diffractive dijet DIS measurements [3, 4, 6] and DPDF fits [2, 3, 8] have been performed for $|t_{\min}| < |t| < 1\ \mathrm{GeV}^2$. To compare with these results, the cross sections are extrapolated to the range $|t_{\min}| < |t| < 1\ \mathrm{GeV}^2$ using the t dependence measured in inclusive diffractive DIS with a leading proton in the final state [15].

4.3.3 Jet selection

Reconstructed hadronic final state objects are used as input to the longitudinally invariant k_T jet algorithm [49] using the p_T recombination scheme with a jet radius of 1.0 as implemented in the FastJet package [50]. The jet finding algorithm is applied in the photon-proton centre-of-mass system ($\gamma^* p$ frame). The jet variables in the $\gamma^* p$ frame are denoted by a asterisk.

In the 'two central jets' analysis, the requirements are $P^*_{T,1} > 5$ GeV and $P^*_{T,2} > 4$ GeV for the leading and next-to-leading jet, respectively. Asymmetric cuts are placed on the jet transverse momenta to restrict the phase space to a region where NLO calculations are reliable. The axes of the jets are required to lie within the pseudorapidity range $-1 < \eta_{1,2} < 2.5$ in the laboratory frame. The selected event topology is similar to that in the LRG dijet data used in the DPDF fits [3, 8]. This data selection is used for testing the proton vertex factorisation hypothesis and the DPDFs in processes with a leading proton in the final state.

The selection of the 'one central + one forward jet' topology is motivated by the study of diffractive DIS processes in a phase space where deviations from DGLAP parton evolution may be present. The requirement of a forward jet suppresses the parton p_T ordering which is assumed by DGLAP evolution. At least one central jet with $-1 < \eta_c < 2.5$ and one forward jet with $1 < \eta_f < 2.8$, where $\eta_f > \eta_c$, are required with $P^*_T > 3.5$ GeV. In addition, the invariant mass of the central-forward jet system is required to be larger than 12 GeV to avoid the phase space region in which NLO QCD calculations are unreliable.

Table 1 Phase space of the diffractive dijet FPS measurements

Selection	Two central jets	One central + one forward jet
DIS	$4 < Q^2 < 110\ \mathrm{GeV}^2$	
	$0.05 < y < 0.7$	
Leading Proton	$x_{\mathbb{P}} < 0.1$	
	$\lvert t\rvert < 1\ \mathrm{GeV}^2$	
Jets	$P^*_{T,1} > 5$ GeV	$P^*_{T,c}, P^*_{T,f} > 3.5$ GeV
	$P^*_{T,2} > 4$ GeV	$M_{jj} > 12$ GeV
	$-1 < \eta_{1,2} < 2.5$	$-1 < \eta_c < 2.5$
		$1 < \eta_f < 2.8,\ \eta_f > \eta_c$

The selection criteria for the two analyses are summarised in Table 1. The 'two central jets' data sample contains 581 events and the 'one central + one forward jet' data sample contains 309 events.

5 Corrections to the data and cross section determination

5.1 Background subtraction

The selected data samples contain background events arising from random coincidences of non-diffractive DIS events, with off-momentum beam-halo protons producing a signal in the FPS. The beam-halo background contribution is estimated statistically by combining the quantity $\sum(E + P_z)$ summed over all reconstructed particles in the central detector in DIS events (without the requirement of a track in the FPS) with the quantity $\sum(E + P_z)$ for beam-halo protons from randomly triggered events. The $\sum(E + P_z)$ spectra for leading proton and beam-halo DIS events for both dijet event topologies are shown in Fig. 2. The background distribution is normalised to the FPS DIS data distribution in the range $\sum(E + P_z) > 1880$ GeV where the beam-halo background dominates. The ratio of signal to background depends on the signal cross section and is found to be considerably larger than in the inclusive diffractive DIS processes measured with the FPS detector [16]. After the selection cut $\sum(E + P_z) < 1880$ GeV the remaining background amounts on average to about 5 %. The background is determined and subtracted bin-by-bin using this method.

5.2 Detector simulation

Monte Carlo simulations are used to correct the data for the effects of detector acceptance, inefficiencies, migrations between measurement intervals due to finite resolution and QED radiation. The response of the H1 detector is simulated in detail using the GEANT3 program [51] and the events are passed through the same analysis chain as is used for the data. The reaction $ep \to eXp$ is simulated with the RAPGAP program [19] using the RP model and the DPDF set H1 2006 Fit B as described in Sect. 3. QED radiative effects are simulated using the HERACLES [52] program within the RAPGAP event generator. In the 'two central jets' analysis the η_2^* distribution of the Monte Carlo simulation is reweighted in order to describe the experimental data. A similar procedure is applied to the η_f^* distribution in the 'one central + one forward jet' sample. More details of the analysis can be found elsewhere [53].

A comparison of the FPS data and the RAPGAP simulation is presented in Fig. 3 for the variables $x_{\mathbb{P}}$ and $|t|$ reconstructed with the FPS detector. The contributions of light quarks (uds) to $\mathbb{P}$ and $\mathbb{R}$ exchanges and of charm quarks to $\mathbb{P}$ exchange are also shown in the $\log_{10}(x_{\mathbb{P}})$ distribution. Figure 4 presents the data and the Monte Carlo distributions of the variables $P_{T,1}^*$, $|\Delta\eta^*|$ and $z_{\mathbb{P}}$ for the 'two central jets' sample and of the variables $\langle P_T^*\rangle$, η_f and $z_{\mathbb{P}}$ for the 'one central + one forward jet' topology. For this comparison $z_{\mathbb{P}}$ is reconstructed from the scattered electron and the hadronic final state in the H1 detector. The MC simulation reproduces the data within the experimental systematic uncertainties. The average detector resolutions on the reconstructed jet variables η, P_T^* and $z_{\mathbb{P}}$ are 7 %, 13 % and 32 %, respectively.

5.3 Cross section determination

In order to account for migration and smearing effects and to evaluates the dijet cross sections at the level of stable hadrons, matrix unfolding of the reconstructed data is performed [54]. The resolution and acceptance of the H1 detector is reflected in the unfolding matrix $\mathbf{A}$ which relates reconstructed variables $\vec{y}_{\text{rec}}$ with variables on the level of stable hadrons $\vec{x}_{\text{true}}$ via the formula $\mathbf{A}\vec{x}_{\text{true}} = \vec{y}_{\text{rec}}$. The matrix $\mathbf{A}$, obtained for each measured distribution using the RAPGAP simulation, is constructed within an enlarged phase space in order to take into account possible migrations from outside of the measured kinematic range. The following sources of migrations to the analysis phase space

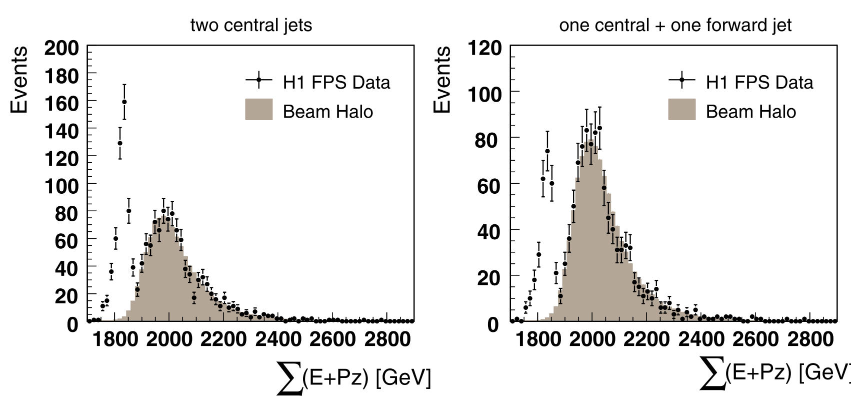

Fig. 2 The distribution of $\sum(E+P_z)$ for FPS DIS events (*points with error bars*) and for beam-halo DIS events (*histogram*)

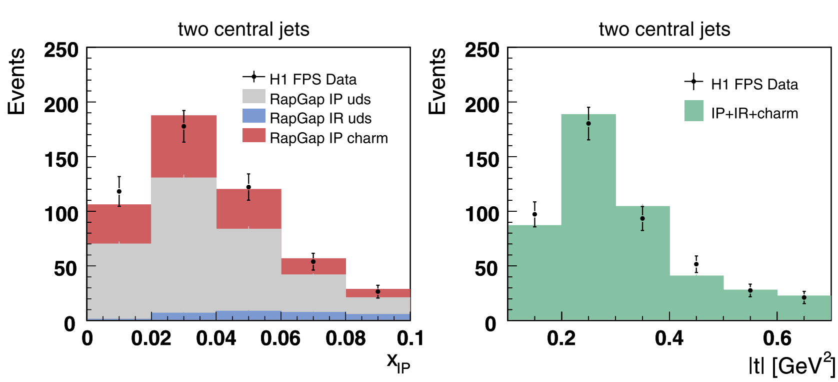

Fig. 3 The distributions of the variables $x_{\mathbb{P}}$ (**a**) and $|t|$ (**b**) reconstructed using the FPS (*points with error bars*) for events with two central jets. The beam-halo background is subtracted from the data. The RAPGAP Monte Carlo simulation, reweighted to describe the η_2^* distribution, is shown as a histogram. Contributions from sub-processes are illustrated in the $x_{\mathbb{P}}$ distribution as areas filled with different colours

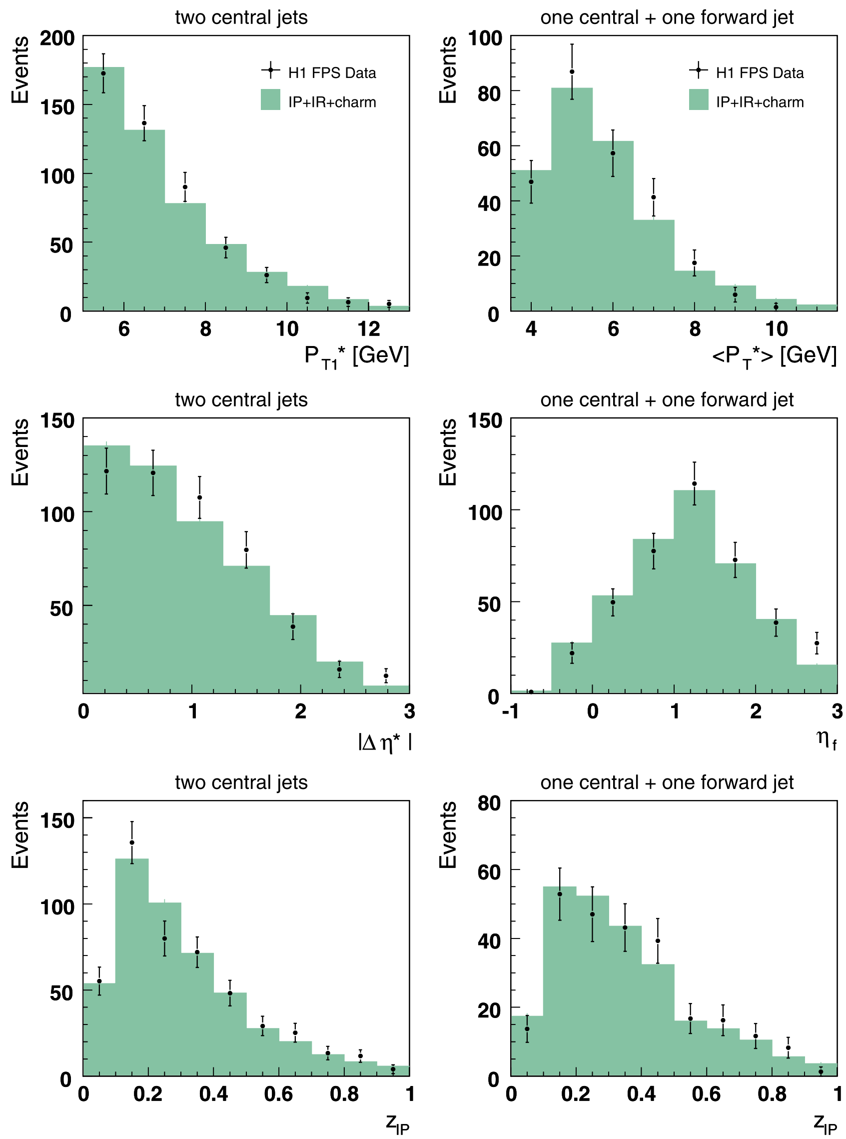

Fig. 4 The distributions of the variables $P_{T,1}^*$, $|\Delta\eta^*|$ and $z_{\mathbb{P}}$ for events with two central jets and of the variables $\langle P_T^*\rangle$, η_2 and $z_{\mathbb{P}}$ for events with one central and one forward jet (*points with the error bars*). The beam-halo background is subtracted from the data. The Rapgap Monte Carlo simulation is shown as histogram

are considered: migrations from low Q^2, from low y, from large $x_{\mathbb{P}}$, from low P_T jets, from the single jet topology, fulfilling the P_T requirements for the leading jet as given in Table 1, and in case of the 'one central + one forward jet' analysis from large η_f. In order to treat the contamination of the measurement by these migrations correctly the analysis is performed in an extended phase space which includes side-bins in $\vec{y}_{\text{rec}}$ and $\vec{x}_{\text{true}}$ for each of the migration sources listed above.

The unfolded true distribution on the level of stable hadrons is obtained from the measured one by minimising a χ^2 function defined as

$$\chi^2 = \chi_A^2 + \tau^2\chi_L^2 = 1/2(\vec{y}_{\text{rec}} - \mathbf{A}\vec{x}_{\text{true}})^T \mathbf{V}^{-1} \times (\vec{y}_{\text{rec}} - \mathbf{A}\vec{x}_{\text{true}}) + \tau^2\chi_L^2 \tag{9}$$

where χ_A^2 is a measure of a deviation of $\mathbf{A}\vec{x}_{\text{true}}$ from the data bins $\vec{y}_{\text{rec}}$. The matrix $\mathbf{V}$ is the covariance matrix of the data, based on the statistical uncertainties. In order to avoid statistical fluctuations, the regularisation term χ_L^2 is implemented into the χ^2 function and defined as $\chi_L^2 = (\vec{x}_{\text{true}})^2$. The regularisation parameter τ is tuned in order to minimise the bin-to-bin correlations of the covariance matrix $\mathbf{V}$. Further details of the unfolding method can be found in [55, 56].

The Born level cross section is calculated in each bin i according to the formula:

$$\sigma_i(ep \to ejjX'p) = \frac{x_i}{\mathcal{L}}(1+\delta_{\text{rad}}). \tag{10}$$

where x_i is the number of background subtracted events as obtained with the unfolding procedure described above, $\mathcal{L}$ is the total integrated luminosity and $(1+\delta_{\text{rad}})$ are the QED radiative corrections which amount to about 5 % on average. The differential cross sections are obtained by dividing by the bin width.

6 Systematic uncertainties on the measured cross sections

The systematic uncertainties are implemented into the response matrix **A** and propagated through the unfolding procedure. They are considered from the following sources listed below.

- The uncertainties on the leading proton energy and on the horizontal and vertical projections of the proton transverse momentum are 1 GeV, 10 MeV and 30 MeV, respectively (Sect. 4.1). The corresponding average uncertainties on the cross section measurements are 0.5 %, 5.3 % and 2.2 %. The dominant uncertainty originates from the FPS acceptance variation as a function of the leading proton transverse momentum in the horizontal projection. The above uncertainties result from the run-by-run variations of the incoming proton beam angle and of the FPS detector positions relative to the proton beam, as well as from the imperfect knowledge of the HERA beam magnet optics.
- The uncertainties of the measurements of the scattered electron energy E'_e (1 %) and angle θ'_e (1 mrad) on the SpaCal calorimeter lead to an average systematic uncertainty of the cross section of 1.5 % and 2.8 %, respectively.
- The systematic uncertainty arising from the hadronic final state reconstruction is determined by varying the energy scale of the hadronic final state by ± 2 % as obtained using a dedicated calibration [57]. The 2 % uncertainty of the calibration is confirmed by studies in the region of low jet transverse momenta and low photon virtuality. This source leads to an average uncertainty of the cross section measurements of 6.2 % for production of two central jets and 9.5 % for production of one central and one forward jet.
- The model dependence of the acceptance and migration corrections is estimated by varying the shapes of the distributions in the kinematic variables $\langle P_T^*\rangle$, η_2^*, η_f^*, $x_{\mathbb{P}}$, β and Q^2 in the RAPGAP simulation within the constraints imposed on those distributions by the presented data. The η_2^* and η_f^* reweightings are varied within the errors of the parameters of the reweighting function, which amount up to a factor 4. The $\langle P_T^*\rangle$ distribution is reweighted by $\langle P_T^*\rangle^{\pm 0.15}$, the $x_{\mathbb{P}}$ distribution by $(1/x_{\mathbb{P}})^{\pm 0.05}$, the β distribution by $\beta^{\pm 0.05}$ and $(1-\beta)^{\mp 0.05}$ and the Q^2 distribution by $\log(Q^2)^{\pm 0.2}$. For the 'two central jets' selection the largest uncertainty is introduced by the η_2^* reweighting (4 %), followed by β (2.7 %), while the reweights in $x_{\mathbb{P}}$, $\langle P_T^*\rangle$ and Q^2 result in an overall uncertainty of 2.3 %. The uncertainties for the 'one central + one forward jet' topology are 12.8 % for the η_f^* reweighting, followed by $\langle P_T^*\rangle$ (2.1 %), while the reweights in $x_{\mathbb{P}}$, β and Q^2 result in an overall uncertainty of 1.8 %.
- Reweighting the t distribution by $e^{\pm t}$ results in a normalisation uncertainty of 4.2 % for the extrapolation in t from the measured range of $0.1 < |t| < 0.7$ GeV^2 to the region $|t_{\min}| < |t| < 1$ GeV^2 covered by the LRG data [3]. The uncertainty arising from the t reweighting within the FPS acceptance range of $0.1 < |t| < 0.7$ GeV^2 is on average 1.4 %.

The following uncertainties are considered to influence the normalisation of all measured cross sections in a correlated way:

- Two sources of systematics related to the background subtraction are taken into account: the energy scale uncertainty and the limited statistics in the data sample without the $\sum(E + p_z)$ cut. Firstly, the beam-halo spectrum is shifted within the quoted uncertainties of the hadronic energy scale and proton energy scale. Secondly, the normalisation of the background spectrum is shifted by $1 \pm 1/\sqrt{N_{\rm bkg}}$, where $N_{\rm bkg}$ is the number of events in the FPS data sample in the range $\sum(E+P_z) > 1880$ GeV. The uncertainties from these two sources are combined in quadrature. The uncertainty of the proton beam-halo background is considered as a normalisation error and found to be 3.5 % for the production of two central jets and 1.5 % for the production of one central and one forward jet.
- A normalisation uncertainty of 1 % is attributed to the trigger efficiencies, evaluated using event samples obtained with independent triggers.
- The uncertainty in the FPS track reconstruction efficiency results in a normalisation uncertainty of 2 %.
- A normalisation uncertainty of 3.7 % arises from the luminosity measurement.

The systematic errors shown in the figures are obtained by adding in quadrature all the contributions except for the normalisation uncertainties, leading to an average uncertainty of 11 % for 'two central jets' and 17 % for 'one central + one forward jet'. The overall normalisation uncertainty of the cross section measurement obtained by adding in quadrature all normalisation uncertainties is 7 % for 'two central jets' and 6.2 % for 'one central + one forward jet'. The cross section measurement in t has a normalisation uncertainty 4.6 %.

7 Results

The *ep* cross section for diffractive production of two central jets and one central + one forward jet, integrated over the full measured kinematic range (Table 1), is given in Table 2 together with the predictions obtained with NLO QCD calculations.

Table 2 Total cross section for the 'two central jets' and 'one central + one forward jet' samples compared to the NLO QCD calculations

	Two central jets σ [pb]	One central + one forward jet σ [pb]
Data	254 ± 20 (stat.) ± 27 (syst.)	150 ± 19 (stat.) ± 26 (syst.)
NLO QCD		
H1 2006 Fit B	$270\,^{+99}_{-57}$ (scale) $^{+30}_{-12}$ (DPDF) ± 16 (hadr.)	148^{+69}_{-38} (scale)$^{+13}_{-5}$ (DPDF) ± 6 (hadr.)
H1 2007 Jets	257^{+77}_{-46} (scale) ± 22 (hadr.)	128^{+55}_{-31} (scale) ± 7 (hadr.)

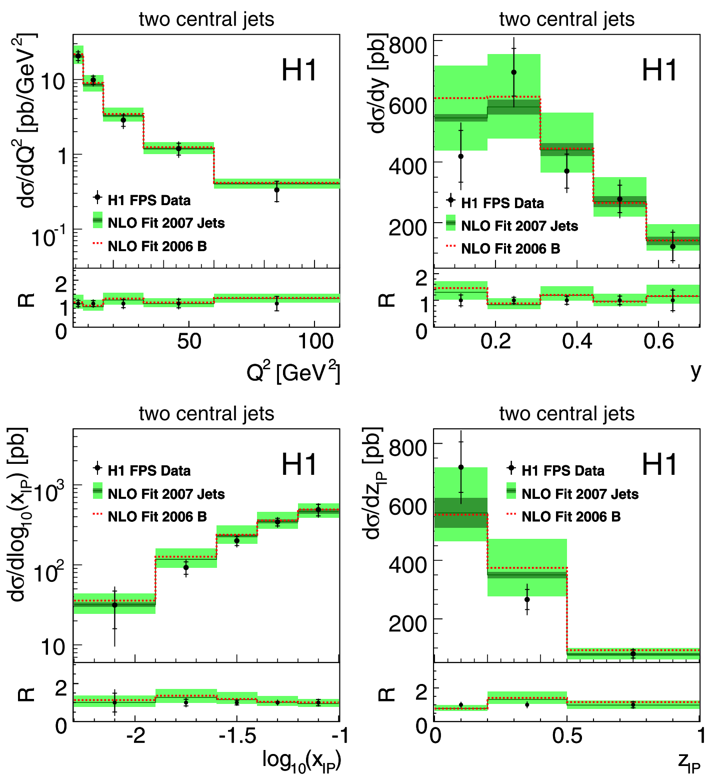

Fig. 5 The differential cross section for the production of two central jets shown as a function of Q^2, y, $\log_{10}(x_{\mathbb{P}})$ and $z_{\mathbb{P}}$. The inner error bars represent the statistical errors. The outer error bars indicate the statistical and systematic errors added in quadrature. NLO QCD predictions based on the DPDF set H1 2007 Jets, corrected to the level of stable hadrons, are shown as a *solid line* and a *dark shaded band* indicating the hadronisation uncertainties and *light shaded band* indicating the hadronisation and scale uncertainties added in quadrature. The NLO calculations based on the DPDF set H1 2006 Fit B with applied hadronisation corrections are shown as a *dashed line*. R denotes the ratio of the measured cross sections and QCD predictions to the nominal values of the measured cross sections. The total normalisation error of 7.0 % is not shown

Within the uncertainties, both cross sections are well described by the NLO QCD calculations.

The measured differential cross sections are presented in Tables 3, 4 and 5 and Figs. 5–14. The tables also include the full covariance matrices of the experimental uncertainties. The quoted differential cross sections are averaged over the intervals specified in the Tables 3, 4 and 5.

7.1 Differential cross section for the production of two central jets

The measured differential cross sections are shown as a function of Q^2, y, $\log_{10}(x_{\mathbb{P}})$ and $z_{\mathbb{P}}$ in Fig. 5. The calculations obtained with the DPDF sets H1 2006 Fit B and H1 2007 Jets are presented as well as the ratio R of the calculations to the data. Within the uncertainties, the normalisation and shape of the cross sections are reasonably well described by the NLO QCD predictions. The NLO QCD predictions are shown with the hadronisation uncertainties and the scale uncertainties, which dominate over the DPDF uncertainties. Since dijet production is directly sensitive to the gluon DPDF, the measured cross sections confirm the normalisation and shape of the gluon DPDFs extracted from the NLO QCD fits to diffractive inclusive and dijet cross sections measured using the LRG method [2, 3].

In Fig. 6 the differential cross sections are shown as a function of $P^*_{T,1}$ and $|\Delta\eta^*|$. Within the errors, NLO QCD predictions describe the data. A slight deviation of the theory from the data is observed for jets with a small separation in pseudorapidity $|\Delta\eta^*|$. The LO QCD contribution is calculated as well using the DPDF set H1 2007 Jets and is observed to underestimate the measured cross section by a factor of about 2.

Figure 7 shows a comparison of the differential cross sections in Q^2, y, $\log_{10}(x_{\mathbb{P}})$ and $z_{\mathbb{P}}$ with MC models based

Table 3 Bin averaged hadron level differential cross sections for diffractive production of two central jets in DIS as a function of Q^2, y, $\log_{10}(x_{\mathbb{P}})$ and $z_{\mathbb{P}}$. The total ($\delta_{\rm tot}$), statistical ($\delta_{\rm stat}$) and systematic ($\delta_{\rm sys}$) uncertainties, the correlation coefficients ρ of the cross section covariance matrix defined in Sect. 5.3, the changes of the cross sections due to a $+1\sigma$ variation of the various systematic error sources described in Sect. 6: the electromagnetic energy scale ($\delta_{\rm ele}$); the scattering angle of the electron (δ_θ); the leading proton energy E_p (δ_{E_p}), the proton transverse momentum components P_x (δ_{P_x}) and P_y (δ_{P_y}); the reweighting of the simulation in η_2 (δ_{η_2}) and $x_{\mathbb{P}}$ ($\delta_{x_{\mathbb{P}}}$) the hadronic energy scale ($\delta E_{\rm had}$); the reweighting of the simulation in β (δ_β), Q^2 (δ_{Q^2}) and P_T^* ($\delta_{P_T^*}$) are given. All uncertainties are given in per cent. The normalisation uncertainty of 7 % is not included. The hadronisation correction factors ($1+\delta_{\rm had}$) applied to the NLO calculations and the associated uncertainty are given in column 21

Q^2 [GeV^2]	$d\sigma/dQ^2$ [pb/GeV^2]	$\delta_{\rm tot}$ [%]	$\delta_{\rm stat}$ [%]	$\delta_{\rm syst}$ [%]	$\rho_{i,i+1}$	$\rho_{i,i+2}$	$\rho_{i,i+3}$	$\rho_{i,i+4}$	δ_{E_e} [%]	δ_{θ_e} [%]	δ_{E_p} [%]	δ_{P_x} [%]	δ_{P_y} [%]	$\delta_{\eta_2^*}$ [%]	$\delta_{x_{\mathbb{P}}}$ [%]	$\delta_{E_{\rm had}}$ [%]	δ_β [%]	δ_{Q^2} [%]	$\delta_{P_T^*}$ [%]	$1+\delta_{\rm had}$
4.0–8.0	21	17.0	13.2	10.6	0.628	0.643	0.596	0.268	−0.5	−3.4	0.2	5.6	−1.8	9.3	1.7	−7.4	−0.2	1.4	2.7	0.87 ± 0.05
8.0–16.0	9.8	14.8	12.5	7.9	0.646	0.588	0.272	–	−1.4	−3.0	0.3	4.6	−2.2	7.6	1.6	4.3	1.0	0.5	1.8	0.88 ± 0.05
16.0–32.0	2.9	20.2	17.3	10.5	0.605	0.256	–	–	0.9	−5.0	−0.2	−5.3	−2.3	11.3	2.0	6.4	−0.9	1.3	2.1	0.89 ± 0.03
32.0–60.0	1.2	20.1	18.1	8.9	0.221	–	–	–	1.0	−1.6	0.1	−5.7	−0.9	−12.2	2.1	5.9	0.7	1.4	1.1	0.89 ± 0.02
60.0–110.0	0.3	31.6	30.6	8.2	–	–	–	–	0.6	−3.1	0.0	4.2	−2.5	2.5	1.4	5.3	−1.4	0.3	1.2	0.89 ± 0.02
y	$d\sigma/dy$ [pb]	$\delta_{\rm tot}$ [%]	$\delta_{\rm stat}$ [%]	$\delta_{\rm syst}$ [%]	$\rho_{i,i+1}$	$\rho_{i,i+2}$	$\rho_{i,i+3}$	$\rho_{i,i+4}$	δ_{E_e} [%]	δ_{θ_e} [%]	δ_{E_p} [%]	δ_{P_x} [%]	δ_{P_y} [%]	$\delta_{\eta_2^*}$ [%]	$\delta_{x_{\mathbb{P}}}$ [%]	$\delta_{E_{\rm had}}$ [%]	δ_β [%]	δ_{Q^2} [%]	$\delta_{P_T^*}$ [%]	$1+\delta_{\rm had}$
0.05–0.18	419	24.6	20.4	13.7	0.506	0.427	0.366	0.224	7.0	−3.0	−0.1	5.9	−2.3	6.2	0.4	7.8	4.7	−0.2	2.9	0.83 ± 0.02
0.18–0.31	696	13.8	11.3	8.0	0.557	0.579	0.449	–	0.6	−1.5	0.1	−4.6	−1.3	8.6	1.4	5.3	2.4	0.1	1.4	0.86 ± 0.04
0.31–0.44	370	17.8	15.2	9.3	0.439	0.335	–	–	−2.8	1.6	0.1	6.8	−0.7	5.5	2.0	5.2	2.4	−0.2	1.1	0.90 ± 0.04
0.44–0.57	279	18.6	16.3	9.1	0.366	–	–	–	2.5	−2.4	0.2	−6.4	3.6	−11.4	2.0	3.1	−0.6	−0.6	1.2	0.97 ± 0.06
0.57–0.70	122	39.7	38.4	10.0	–	–	–	–	−6.3	−1.1	0.1	−5.7	−0.8	18.9	2.9	−2.4	2.5	−0.1	1.7	0.98 ± 0.10
$\log_{10}(x_{\mathbb{P}})$	$d\sigma/d\log_{10}(x_{\mathbb{P}})$ [pb]	$\delta_{\rm tot}$ [%]	$\delta_{\rm stat}$ [%]	$\delta_{\rm syst}$ [%]	$\rho_{i,i+1}$	$\rho_{i,i+2}$	$\rho_{i,i+3}$	$\rho_{i,i+4}$	δ_{E_e} [%]	δ_{θ_e} [%]	δ_{E_p} [%]	δ_{P_x} [%]	δ_{P_y} [%]	$\delta_{\eta_2^*}$ [%]	$\delta_{x_{\mathbb{P}}}$ [%]	$\delta_{E_{\rm had}}$ [%]	δ_β [%]	δ_{Q^2} [%]	$\delta_{P_T^*}$ [%]	$1+\delta_{\rm had}$
−2.3–(−1.9)	32	57.0	49.5	28.2	−0.240	0.179	0.161	0.056	5.9	3.3	24.0	6.2	13.3	−5.9	1.7	−18.9	0.9	−0.7	0.4	0.96 ± 0.06
−1.9–(−1.6)	93	20.2	17.6	10.0	0.136	−0.027	−0.047	–	1.3	−1.1	−8.4	−6.0	−0.6	−5.4	−0.6	5.0	0.4	0.7	2.0	0.91 ± 0.01
−1.6–(−1.4)	200	15.9	12.8	9.5	0.579	0.334	–	–	1.1	−1.9	−3.8	6.0	−1.2	0.4	0.1	5.5	−0.4	0.2	1.8	0.89 ± 0.03
−1.4–(−1.2)	344	13.9	11.0	8.6	0.709	–	–	–	0.4	−1.7	−4.3	−4.9	−2.5	4.4	−0.7	4.2	−0.2	0.2	1.9	0.87 ± 0.05
−1.2–(−1.0)	488	18.8	16.5	9.0	–	–	–	–	−0.3	−2.1	−5.6	−4.4	−0.8	5.8	−1.7	3.8	0.7	0.1	2.6	0.87 ± 0.06
$z_{\mathbb{P}}$	$d\sigma/dz_{\mathbb{P}}$ [pb]	$\delta_{\rm tot}$ [%]	$\delta_{\rm stat}$ [%]	$\delta_{\rm syst}$ [%]	$\rho_{i,i+1}$	$\rho_{i,i+2}$			δ_{E_e} [%]	δ_{θ_e} [%]	δ_{E_p} [%]	δ_{P_x} [%]	δ_{P_y} [%]	$\delta_{\eta_2^*}$ [%]	$\delta_{x_{\mathbb{P}}}$ [%]	$\delta_{E_{\rm had}}$ [%]	δ_β [%]	δ_{Q^2} [%]	$\delta_{P_T^*}$ [%]	$1+\delta_{\rm had}$
0.0–0.2	719	14.7	12.0	8.5	0.601	0.127			−1.5	−2.4	5.6	−4.5	2.3	−8.4	0.2	−1.5	0.7	0.6	1.9	0.88 ± 0.08
0.2–0.5	266	16.5	12.9	10.3	0.336	–			−1.4	−1.6	2.0	6.7	1.9	10.1	1.6	6.3	2.3	0.1	1.4	0.88 ± 0.03
0.5–1.0	80	22.3	17.8	13.4	–	–			−3.2	−1.8	6.4	4.7	5.0	4.2	−1.5	8.3	2.1	0.0	0.5	0.90 ± 0.05

Table 4 Bin averaged hadron level differential cross sections for diffractive production of two central jets in DIS as a function of $p^*_{T,1}$, $|\Delta\eta^*|$ and $|t|$. The normalisation uncertainty of 4.6 % for the differential cross section in $|t|$ and 7 % for other cross sections is not included. For details see Table 3

p^*_{T1} [GeV]	$d\sigma/dp^*_{T1}$ [pb/GeV]	δ_{tot} [%]	δ_{stat} [%]	δ_{syst} [%]	$\rho_{i,i+1}$	$\rho_{i,i+2}$		δ_{E_e} [%]	δ_{θ_e} [%]	δ_{E_p} [%]	δ_{P_x} [%]	δ_{P_y} [%]	$\delta_{\eta^*_2}$ [%]	$\delta_{x_{\mathbb{P}}}$ [%]	$\delta_{E_{\mathrm{had}}}$ [%]	δ_β [%]	δ_{Q^2} [%]	$\delta_{P^*_T}$ [%]	$1+\delta_{\mathrm{had}}$
5.0–6.5	91	17.6	15.3	8.6	0.402	0.180		1.7	−3.2	0.2	−5.4	2.4	−6.8	2.1	−2.2	3.5	−0.5	2.2	0.81 ± 0.04
6.5–8.5	44	17.0	13.2	10.8	0.395	–		−0.7	0.6	−0.3	6.6	3.2	9.6	1.6	7.3	2.1	0.2	0.7	0.96 ± 0.05
8.5–12.0	7.3	39.1	33.0	20.9	–	–		3.2	−5.8	−2.0	1.7	4.0	13.9	2.4	19.4	−0.5	0.1	0.5	0.99 ± 0.04
$\|\Delta\eta^*\|$	$d\sigma/d\|\Delta\eta^*\|$ [pb]	δ_{tot} [%]	δ_{stat} [%]	δ_{syst} [%]	$\rho_{i,i+1}$	$\rho_{i,i+2}$	$\rho_{i,i+3}$	δ_{E_e} [%]	δ_{θ_e} [%]	δ_{E_p} [%]	δ_{P_x} [%]	δ_{P_y} [%]	$\delta_{\eta^*_2}$ [%]	$\delta_{x_{\mathbb{P}}}$ [%]	$\delta_{E_{\mathrm{had}}}$ [%]	δ_β [%]	δ_{Q^2} [%]	$\delta_{P^*_T}$ [%]	$1+\delta_{\mathrm{had}}$
0.0–0.6	118	16.1	13.2	9.2	0.682	0.276	−0.479	−0.6	−2.3	0.1	−5.7	−1.6	−14.9	1.8	5.7	1.9	−0.3	1.5	0.88 ± 0.04
0.6–1.2	157	14.2	11.5	8.3	0.343	−0.342	–	1.2	−1.7	0.0	5.0	2.8	−8.7	1.6	4.8	2.0	−0.1	1.3	0.89 ± 0.04
1.2–1.8	97	19.8	17.4	9.4	0.089	–	–	1.1	−2.3	0.1	−4.8	−2.1	2.2	1.7	6.1	−2.6	0.0	1.7	0.90 ± 0.04
1.8–3.0	26	33.3	31.8	9.8	–	–	–	2.0	2.8	0.3	−5.1	−0.7	−32.9	0.5	4.3	4.7	0.6	3.1	0.84 ± 0.02
$\|t\|$ [GeV^2]	$d\sigma/d\|t\|$ [pb/GeV^2]	δ_{tot} [%]	δ_{stat} [%]	δ_{syst} [%]	$\rho_{i,i+1}$	$\rho_{i,i+2}$		δ_{E_e} [%]	δ_{θ_e} [%]	δ_{E_p} [%]	δ_{P_x} [%]	δ_{P_y} [%]	$\delta_{\eta^*_2}$ [%]	$\delta_{x_{\mathbb{P}}}$ [%]	$\delta_{E_{\mathrm{had}}}$ [%]	δ_β [%]	δ_{Q^2} [%]	$\delta_{P^*_T}$ [%]	
0.1–0.3	483	17.3	9.3	14.6	0.495	0.420		−0.5	−1.5	−0.3	10.3	3.8	12.8	1.9	9.2	1.0	0.3	0.6	
0.3–0.5	151	16.6	12.5	11.0	0.288	–		0.5	1.9	−0.1	−4.6	3.1	8.6	1.6	9.0	0.6	−0.3	0.8	
0.5–0.7	44	29.5	25.9	14.0	–	–		2.3	−1.8	1.1	−3.6	10.4	−11.4	−1.0	−8.0	0.0	0.2	1.0	

Table 5 Bin averaged hadron level differential cross sections for diffractive production of one central and one forward jet in DIS as a function of $\langle P_T^* \rangle$, $|\Delta\eta^*|$, η_f, $z_{\mathbb{P}}$, $\log_{10}(\beta)$ and $|\Delta\phi^*|$. The normalisation uncertainty of 6.2 % is not included. For more details see Table 3

$\langle p_T^* \rangle$ [GeV]	$d\sigma/d\langle p_T^* \rangle$ [pb/GeV]	δ_{tot} [%]	δ_{stat} [%]	δ_{syst} [%]	$\rho_{i,i+1}$	$\rho_{i,i+2}$		δ_{E_e} [%]	δ_{θ_e} [%]	δ_{E_p} [%]	δ_{P_x} [%]	δ_{P_y} [%]	$\delta_{\eta_f^*}$ [%]	$\delta_{x_{\mathbb{P}}}$ [%]	$\delta_{E_{had}}$ [%]	δ_β [%]	δ_{Q^2} [%]	$\delta_{P_T^*}$ [%]	$1+\delta_{had}$
3.5–5.0	40	33.0	28.8	16.2	0.433	0.403		−3.5	−0.9	−0.7	4.5	−1.8	11.1	0.6	−14.1	3.6	1.8	1.8	0.7 ± 0.09
5.0–7.0	36	17.3	15.8	7.2	0.577	–		−0.8	−3.9	−0.3	3.2	2.2	12.1	1.0	3.4	−0.9	1.1	1.9	0.93 ± 0.08
7.0–12.0	8.8	26.0	22.9	12.2	–	–		1.3	−2.0	0.4	4.7	−2.2	24.4	1.6	9.9	−1.5	−0.1	0.2	1.05 ± 0.03
$\|\Delta\eta^*\|$	$d\sigma/d\|\Delta\eta^*\|$ [pb]	δ_{tot} [%]	δ_{stat} [%]	δ_{syst} [%]	$\rho_{i,i+1}$	$\rho_{i,i+2}$		δ_{E_e} [%]	δ_{θ_e} [%]	δ_{E_p} [%]	δ_{P_x} [%]	δ_{P_y} [%]	$\delta_{\eta_f^*}$ [%]	$\delta_{x_{\mathbb{P}}}$ [%]	$\delta_{E_{had}}$ [%]	δ_β [%]	δ_{Q^2} [%]	$\delta_{P_T^*}$ [%]	$1+\delta_{had}$
0.0–1.2	21	30.0	28.3	10.2	0.489	0.321		0.6	−3.9	−0.3	4.4	−3.6	20.1	0.0	6.0	0.2	0.7	4.1	1.04 ± 0.07
1.2–2.4	60	20.9	17.3	11.7	0.329	–		−1.8	3.0	0.2	4.0	2.3	10.2	1.3	9.5	2.1	1.6	1.9	0.88 ± 0.07
2.4–3.5	48	26.5	25.0	8.8	–	–		−2.0	−0.8	1.0	4.8	1.6	7.0	0.0	6.7	−0.9	0.4	1.1	0.69 ± 0.06
η_f	$d\sigma/d\eta_f$ [pb]	δ_{tot} [%]	δ_{stat} [%]	δ_{syst} [%]	$\rho_{i,i+1}$	$\rho_{i,i+2}$	$\rho_{i,i+3}$	δ_{E_e} [%]	δ_{θ_e} [%]	δ_{E_p} [%]	δ_{P_x} [%]	δ_{P_y} [%]	$\delta_{\eta_f^*}$ [%]	$\delta_{x_{\mathbb{P}}}$ [%]	$\delta_{E_{had}}$ [%]	δ_β [%]	δ_{Q^2} [%]	$\delta_{P_T^*}$ [%]	$1+\delta_{had}$
−0.6–0.2	23	24.1	21.9	10.0	0.391	0.437	0.360	3.5	−2.3	−0.1	5.5	2.3	−6.4	−1.9	6.5	0.0	0.7	0.5	0.89 ± 0.06
0.2–0.9	63	17.0	14.3	9.2	0.567	0.427	–	−0.5	1.4	−0.1	−6.4	−1.9	8.0	−2.0	5.3	−1.5	0.2	−1.7	0.93 ± 0.05
0.9–1.6	98	15.4	12.5	9.1	0.549	–	–	−0.2	−1.7	0.1	−4.9	−1.7	6.2	1.5	6.9	−0.4	0.7	0.3	0.89 ± 0.04
1.6–2.8	75	21.9	18.5	11.7	–	–	–	−0.7	2.9	−0.4	2.9	−1.0	9.0	−0.2	10.1	−0.5	0.2	3.4	0.86 ± 0.01
$z_{\mathbb{P}}$	$d\sigma/dz_{\mathbb{P}}$ [pb]	δ_{tot} [%]	δ_{stat} [%]	δ_{syst} [%]	$\rho_{i,i+1}$	$\rho_{i,i+2}$		δ_{E_e} [%]	δ_{θ_e} [%]	δ_{E_p} [%]	δ_{P_x} [%]	δ_{P_y} [%]	$\delta_{\eta_f^*}$ [%]	$\delta_{x_{\mathbb{P}}}$ [%]	$\delta_{E_{had}}$ [%]	δ_β [%]	δ_{Q^2} [%]	$\delta_{P_T^*}$ [%]	$1+\delta_{had}$
0.0–0.2	265	33.0	28.1	17.2	0.157	−0.170		−5.7	−2.4	10.4	7.8	−3.0	4.5	−2.3	5.0	8.8	2.5	2.0	0.93 ± 0.10
0.2–0.5	249	23.8	16.7	16.9	0.153	–		−2.4	2.3	5.2	−3.2	3.2	10.8	0.0	−2.3	−2.1	0.8	1.5	0.85 ± 0.08
0.5–1.0	43	51.0	33.4	38.5	–	–		−10.7	−6.7	16.0	4.0	−1.1	28.8	−2.8	22.1	−0.6	0.9	1.2	0.82 ± 0.02
$\log_{10}(\beta)$	$d\sigma/d\log_{10}(\beta)$ [pb]	δ_{tot} [%]	δ_{stat} [%]	δ_{syst} [%]	$\rho_{i,i+1}$	$\rho_{i,i+2}$		δ_{E_e} [%]	δ_{θ_e} [%]	δ_{E_p} [%]	δ_{p_x} [%]	δ_{p_y} [%]	$\delta_{\eta_f^*}$ [%]	$\delta_{x_{\mathbb{P}}}$ [%]	$\delta_{E_{had}}$ [%]	δ_β [%]	δ_{Q^2} [%]	$\delta_{P_T^*}$ [%]	$1+\delta_{had}$
−3.0–(−2.1)	63	29.1	23.4	17.2	0.419	0.115		3.3	−5.2	4.8	−9.6	−3.0	5.2	−1.1	6.0	8.8	3.4	3.0	0.89 ± 0.08
−2.1–(−1.6)	136	18.6	14.9	11.0	0.396	–		−1.4	−1.7	−1.1	3.3	−1.5	12.5	1.2	9.4	1.7	1.7	1.6	0.85 ± 0.07
−1.6–(−0.5)	21	38.4	30.6	23.2	–	–		−5.3	−2.9	−19.8	3.6	5.6	21.9	1.6	−8.4	−1.1	0.1	3.2	0.84 ± 0.05
$\|\Delta\phi^*\|$ [degree]	$d\sigma/d\|\Delta\phi^*\|$ [pb/degree]	δ_{tot} [%]	δ_{stat} [%]	δ_{syst} [%]	$\rho_{i,i+1}$			δ_{E_e} [%]	δ_{θ_e} [%]	δ_{E_p} [%]	δ_{P_x} [%]	δ_{P_y} [%]	$\delta_{\eta_f^*}$ [%]	$\delta_{x_{\mathbb{P}}}$ [%]	$\delta_{E_{had}}$ [%]	δ_β [%]	δ_{Q^2} [%]	$\delta_{P_T^*}$ [%]	$1+\delta_{had}$
0.0–160.0	0.3	41.9	36.4	20.9	0.261			−1.2	−1.8	−2.5	−2.9	−2.9	6.7	−1.0	19.6	3.8	0.7	4.1	0.91 ± 0.16
160.0–180.0	5.2	17.2	14.9	8.7	–			0.2	−1.6	−0.4	4.5	−1.7	16.6	1.3	6.0	1.0	0.8	2.2	0.85 ± 0.05

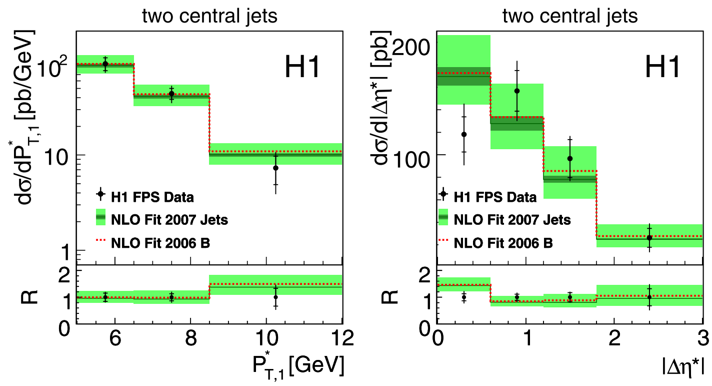

Fig. 6 The differential cross section for production of two central jets shown as a function of $P^*_{T,1}$ and $|\Delta\eta^*|$. For more details see Fig. 5

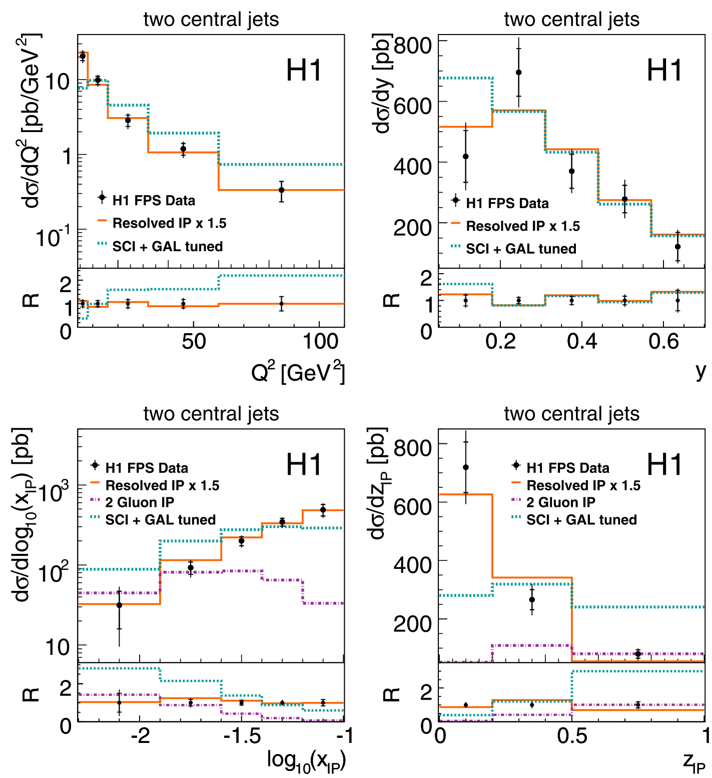

Fig. 7 The differential cross section for the production of two central jets shown as a function of Q^2, y, $\log_{10}(x_{\mathbb{P}})$ and $z_{\mathbb{P}}$. The inner error bars represent the statistical errors. The outer error bars indicate the statistical and systematic errors added in quadrature. The RP, SCI+GAL and TPR models are shown as *solid*, *dotted* and *dashed-dotted lines*, respectively. R denotes the ratio of the measured cross sections and MC model predictions to the nominal values of the measured cross sections. The total normalisation error of 7.0 % is not shown

on the leading-logarithm approximation and parton showers. he ratios of the measured cross sections to the MC predictions show that the RP model gives a good description of the shape, but underestimates the dijet cross section by a factor of 1.5. For this comparison the reweighting with respect to the η_2^* distribution specified in Sect. 5.2 is not applied to the RP model. Since the $\mathbb{P}$ and $\mathbb{R}$ fluxes which determine the $x_{\mathbb{P}}$ dependence in the RP model has been tuned to the inclusive diffractive DIS LRG data [2] the good agreement in shape of the RP model with the dijet data supports the hypothesis of the proton vertex factorisation. Both the SCI+GAL and TGP models fail to describe the data. The SCI+GAL model predicts harder spectra in Q^2 and $z_{\mathbb{P}}$ and a softer spectrum in $\log_{10}(x_{\mathbb{P}})$ than are seen in the data. It should be noted that the probability of soft colour interactions and hence the normalisation of diffractive processes in the SCI+GAL model is adjusted to the measured dijet cross section. The TGP model is in agreement with the data only at low $x_{\mathbb{P}}$ but underestimates the data significantly at larger $x_{\mathbb{P}}$ sub-leading contributions are expected to be large.

Figure 8 shows the differential cross sections in $P^*_{T,1}$ and $|\Delta\eta^*|$ for the data and the MC models. The shapes of these distributions are again well described by the RP model. Although the SCI+GAL model is not able to describe the differential cross sections as a function of the diffractive kinematic variables $x_{\mathbb{P}}$ and $z_{\mathbb{P}}$ and of the DIS kinematic variable Q^2 this model reproduces reasonably well the measurements as a function of the jet variables $P^*_{T,1}$ and $|\Delta\eta^*|$.

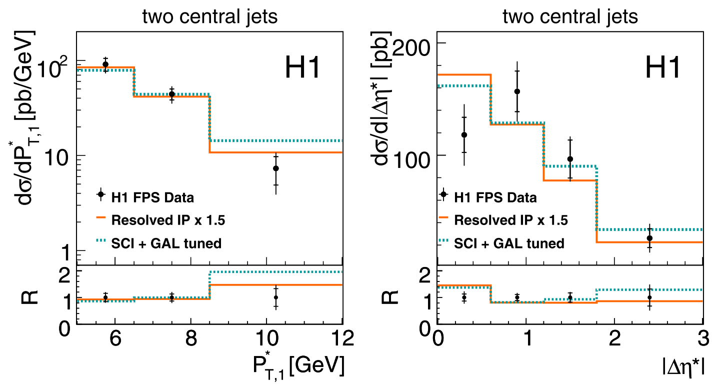

Fig. 8 The differential cross section for production of two central jets shown as a function of $P^*_{T,1}$ and $|\Delta\eta^*|$. For more details see Fig. 7

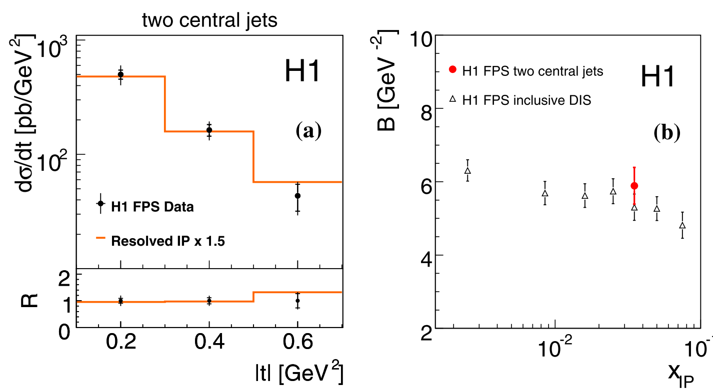

Fig. 9 The differential cross section for production of two central jets shown as a function of t (**a**), the corresponding t-slope (*circle*) shown as a function of $x_{\mathbb{P}}$ (**b**). The result is compared to the H1 inclusive diffractive DIS data (*triangles*) [16]. The error bars indicate the statistical and systematic errors added in quadrature

None of the LO Monte Carlo models are able to describe all features of the measured differential cross sections. The best shape description in all cases is provided by the RP model. However, this model is a factor of 1.5 below the data in normalisation. The TGP and SCI+GAL models fail to describe the shape of the differential cross sections.

The differential cross section in $|t|$ shown in Fig. 9a is fit using an exponential form $\exp(Bt)$ motivated by Regge phenomenology. An iterative procedure is used to determine the slope parameter B, where bin centre corrections are applied to the differential cross section in t using the value of B extracted from the previous fit iteration. The final fit results in $B = 5.89 \pm 0.50$ (exp.) GeV^{-2}, where the experimental uncertainty is defined as the quadratic sum of the statistical and systematic uncertainties and the full covariance matrix is taken into account in the fit. As shown in Fig. 9b, this t-slope parameter is consistent within the errors with the t-slope measured in inclusive diffractive DIS with a leading proton in the final state [16] at the same value of $x_{\mathbb{P}}$. The consistency of the measured t dependence with that for the inclusive diffractive DIS cross sections supports the validity of the proton vertex factorisation hypothesis.

The cross section for the production of two central jets can be compared with the diffractive dijet measurement obtained using the LRG technique [3]. The LRG measurement includes proton dissociation to states Y with masses $M_Y < 1.6$ GeV. To correct for the contributions of proton dissociation processes, the LRG dijet data are scaled down by a factor of 1.20, taken from the diffractive inclusive DIS measurement [16]. To compare to the results of the LRG method, dijet events are selected in the same kinematic range. The DIS and jet variables Q^2, y, $P^*_{T,1}$ and $\eta_{1,2}$ are restricted to the ranges $4 < Q^2 < 80\ \mathrm{GeV}^2$, $0.1 < y < 0.7$, $P^*_{T,1} > 5.5$ GeV, and $-1 < \eta_{1,2} < 2$, respectively. The results are presented in Fig. 10. The comparison shows consistency of the results within the experimental errors. Compared to the LRG measurement, the phase space of the present analysis extends to $x_{\mathbb{P}}$ values that are a factor of three larger.

7.2 Differential cross section for the production of one central + one forward jet

Figure 11 shows the differential cross sections for the production of 'one central + one forward jet' as a function of $|\Delta\eta^*|$, η_f and the mean transverse momentum of the forward and central jets $\langle P^*_T \rangle$ together with the expectations from the NLO QCD. Within the errors, the measured data are described by NLO QCD predictions. The NLO QCD predictions are shown with the hadronisation uncertainties and the scale uncertainties, which dominate over the DPDF uncertainties.

In order to test the predictions in a wider kinematic range, the η_f distribution of the forward jet shown in Fig. 11 is ex-

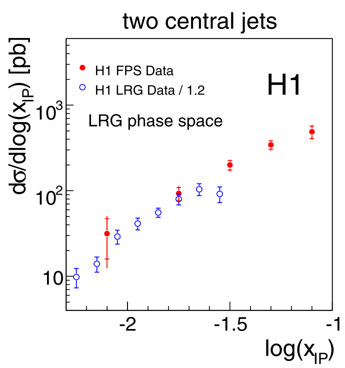

Fig. 10 The differential cross section for the production of two central jets in the phase space of the LRG measurement [3] as described the text in Sect. 7.1. The cross section is shown as a function of $\log_{10}(x_{\mathbb{P}})$. The inner error bars represent the statistical errors. The outer error bars indicate the statistical and systematic errors added in quadrature. The published LRG dijet data are scaled down by a factor of 1.20 to correct for the proton dissociation contribution are shown as *open circles* with the error bars indicating the statistical and systematic errors added in quadrature

tended down to a minimum value of -0.6 where the prediction overshoots the data. LO QCD calculations, performed using the DPDF set H1 2007 Jets underestimate the measured cross section by a factor of about 2.5.

The differential cross sections measured as a function of $z_{\mathbb{P}}$, $\log_{10}(\beta)$ and $|\Delta\phi^*|$ are presented in Fig. 12. The data are well described by the NLO QCD predictions. In the BFKL approach [58–60], additional gluons can be emitted in the gap between the two jets, leading to a de-correlation in azimuthal angle $|\Delta\phi^*|$. The observed agreement between the measured cross sections and NLO DGLAP predictions in this distribution shows no evidence for such an effect in the kinematic region accessible in this analysis.

Figure 13 presents the differential cross sections for the production of 'one central + one forward jet' as a function of the variables $\langle P_T^*\rangle$, $|\Delta\eta^*|$ and η_f. in the case of 'two central jets', The RP model is a factor of 2.2 below the data which is a larger discrepancy in normalisation than that observed in the 'two central jets' sample. A similar trend is seen for the LO QCD contributions in the two samples. The normalisation of the SCI+GAL model, tuned to 'two central jets', agrees with the cross section for 'one central +

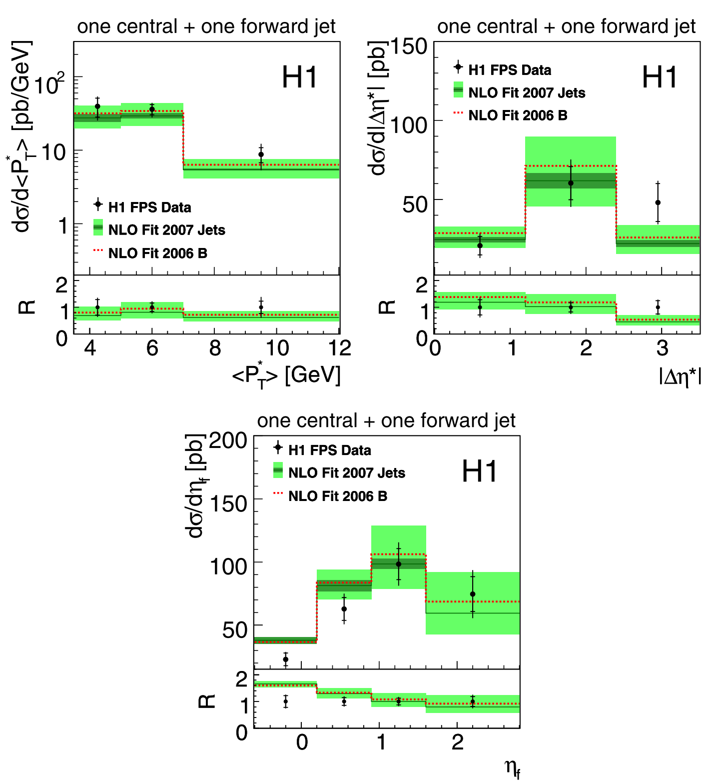

Fig. 11 The differential cross section for the production of one central and one forward jet shown as a function of the mean transverse momentum of two jets $\langle P_T^*\rangle$, $|\Delta\eta^*|$ and η_f. The inner error bars represent the statistical errors. The outer error bars indicate the statistical and systematic errors added in quadrature. NLO QCD predictions based on the DPDF set H1 2007 Jets, corrected to the level of stable hadrons, are shown as a line with a *dark shaded band* indicating the hadronization error and *light shaded band* indicating the hadronization and scale errors added in quadrature. The NLO calculations based on the DPDF set H1 2006 Fit B with applied hadronisation corrections is shown as a *dashed line*. R denotes the ratio of the measured cross sections and QCD predictions to the nominal values of the measured cross sections. The total normalisation error of 6.2 % is not shown

Fig. 12 The differential cross section for production of one central and one forward jet shown as a function of $z_{\mathbb{P}}$, $\log_{10}(\beta)$ and $|\Delta\phi^*|$. For more details see Fig. 11

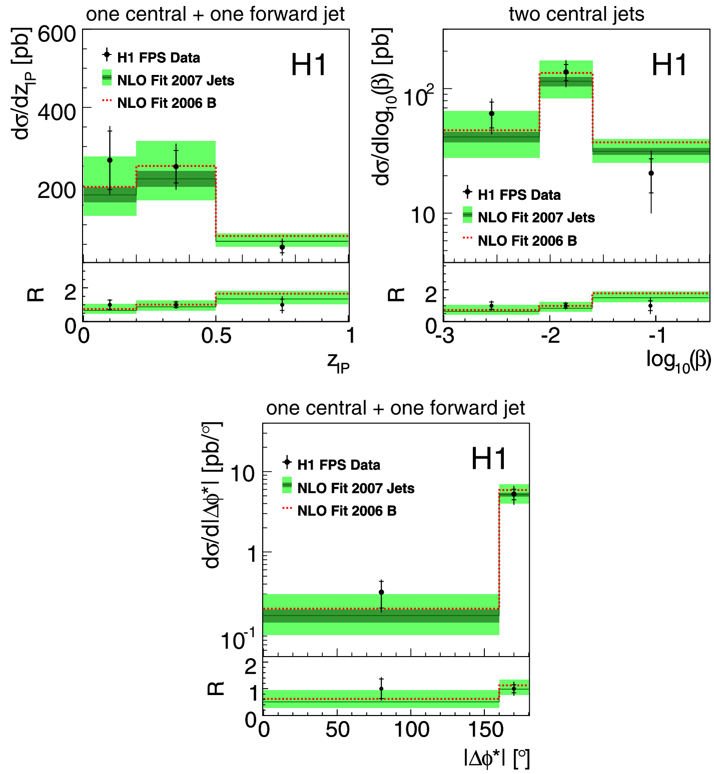

Fig. 13 The differential cross section for production of one central and one forward jet shown as a function of the mean transverse momentum of two jets $\langle P_T^* \rangle$, $|\Delta\eta^*|$ and η_f. The inner error bars represent the statistical errors. The outer error bars indicate the statistical and systematic errors added in quadrature. The RP and the SCI+GAL models are shown as *solid* and *dotted lines*, respectively. R denotes the ratio of the measured cross sections and MC model predictions to the nominal values of the measured cross sections. The total normalisation error of 6.2 % is not shown

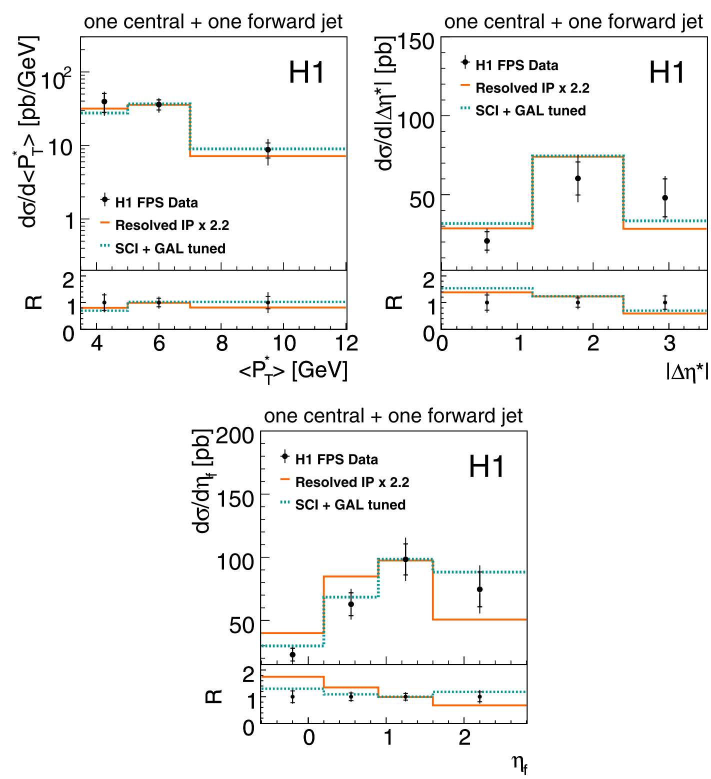

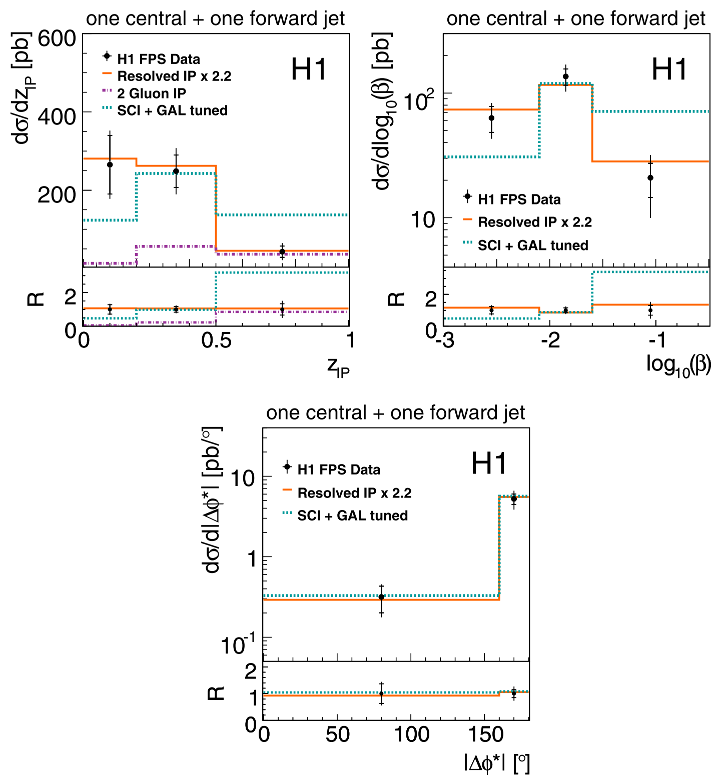

Fig. 14 The differential cross section for production of one central and one forward jet shown as a function of $z_{\mathbb{P}}$, $\log_{10}(\beta)$ and $|\Delta\phi^*|$. The RP, SCI+GAL and TPG models are shown as *full*, *dotted* and *dashed-dotted lines*. For more details see Fig. 13

one forward jet'. The shapes of the distributions are reasonably well described by both the RP and SCI+GAL models.

The differential cross sections in $z_{\mathbb{P}}$, $\log_{10}(\beta)$ and $|\Delta\phi^*|$ are shown in Fig. 14. The shapes of all distributions are well described only by the RP model. As for the case of the 'two central jets' the SCI+GAL model is not able to describe the distributions of the diffractive kinematic variables but it well reproducing the shape of the $|\Delta\phi^*|$ distribution. The TGP model completely fails again to describe the $z_{\mathbb{P}}$ spectrum.

8 Summary

Integrated and differential cross sections are measured for dijet production in the diffractive DIS process $ep \rightarrow ejjX'p$. In the process studied, the scattered proton carries at least 90 % of the incoming proton momentum and is measured in the H1 Forward Proton Spectrometer. The presented results are compatible with the previous measurements based on the LRG method and explore a new domain at large $x_{\mathbb{P}}$.

Dijet cross sections are measured for an event topology with two jets produced in the central pseudorapidity region, where DGLAP parton evolution mechanism is expected to dominates, and for a topology with one jet in the central region and one jet in the forward region, where effects of non-DGLAP parton evolution may be observed. NLO QCD predictions based on the DGLAP approach and using DPDFs extracted from inclusive diffraction measurements describe the dijet cross sections within the errors for both event topologies, supporting the universality of DPDFs. The measured t-slope of the dijet cross section is consistent within uncertainties with the value measured in inclusive diffractive DIS with a leading proton in the final state. This confirms the validity of the proton vertex factorisation hypothesis for dijet production in diffractive DIS.

The measured cross sections are compared with predictions from Monte Carlo models based on leading order matrix elements and parton showers. The Resolved Pomeron model describes the shape of the cross sections well, but is too low in normalisation. This suggests that contributions from higher order processes are expected to be sizable in this approach. The SCI+GAL model is able to reproduce the normalisation of the cross section for both dijet topologies presented after tuning the model to the 'two central jets' data. The dependence of the diffractive dijet cross section on $x_{\mathbb{P}}$ and $z_{\mathbb{P}}$ is able to distinguish between the models. The SCI+GAL and Two Gluon Pomeron models fail to describe the shape of the distributions of the diffractive variables, while the Resolved Pomeron model describes the shape of these distributions well.

Acknowledgements We are grateful to the HERA machine group whose outstanding efforts have made this experiment possible. We thank the engineers and technicians for their work in constructing and maintaining the H1 detector, our funding agencies for financial support, the DESY technical staff for continual assistance and the DESY directorate for support and for the hospitality which they extend to the non-DESY members of the collaboration.

References

1. C. Adloff et al. (H1 Collaboration), Z. Phys. C **76**, 613 (1997). arXiv:hep-ex/9708016
2. A. Aktas et al. (H1 Collaboration), Eur. Phys. J. C **48**, 715 (2006). arXiv:hep-ex/0606004
3. A. Aktas et al. (H1 Collaboration), J. High Energy Phys. **0710**, 042 (2007). arXiv:0708.3217
4. A. Aktas et al. (H1 Collaboration), Eur. Phys. J. C **51**, 549 (2007). arXiv:hep-ex/0703022
5. A. Aktas et al. (H1 Collaboration), Eur. Phys. J. C **50**, 1 (2007). arXiv:hep-ex/0610076
6. S. Chekanov et al. (ZEUS Collaboration), Eur. Phys. J. C **52**, 813 (2007). arXiv:0708.1415
7. S. Chekanov et al. (ZEUS Collaboration), Nucl. Phys. B **816**, 1 (2009). arXiv:0812.2003
8. S. Chekanov et al. (ZEUS Collaboration), Nucl. Phys. B **831**, 1 (2010). arXiv:0911.4119
9. J. Collins, Phys. Rev. D **57**, 3051 (1998) [Erratum-ibid. D **61** (2000) 019902]; arXiv:hep-ph/9709499
10. V. Gribov, L. Lipatov, Sov. J. Nucl. Phys. **15**, 438 (1972) [Yad. Fiz. **15** (1972) 781]
11. V. Gribov, L. Lipatov, Sov. J. Nucl. Phys. **15**, 675 (1972) [Yad. Fiz. **15** (1972) 1218]
12. Y. Dokshitzer, Sov. Phys. JETP **46**, 641 (1977) [Zh. Eksp. Teor. Fiz. **73** (1977) 1216]
13. G. Altarelli, G. Parisi, Nucl. Phys. B **126**, 298 (1977)
14. L. Trentadue, G. Veneziano, Phys. Lett. B **323**, 201 (1994)
15. A. Aktas et al. (H1 Collaboration), Eur. Phys. J. C **48**, 749 (2006). arXiv:hep-ex/0606003
16. A. Aktas et al. (H1 Collaboration), Eur. Phys. J. C **71**, 1578 (2011). arXiv:1010.1476
17. G. Ingelman, P.E. Schlein, Phys. Lett. B **152**, 256 (1985)
18. A. Donnachie, P.V. Landshoff, Phys. Lett. B **191**, 309 (1987)
19. H. Jung, Comput. Phys. Commun. **86**, 147 (1995)
20. J. Owens, Phys. Rev. D **30**, 943 (1984)
21. G.A. Schuler, T. Sjöstrand, Z. Phys. C **68**, 607 (1995). arXiv:hep-ph/9503384
22. J. Bartels, C. Ewerz, H. Lotter, M. Wüsthoff, M. Diehl, Phys. Lett. B **379**, 239 (1996). arXiv:hep-ph/9609239
23. J. Bartels, H. Jung, M. Wüsthoff, Eur. Phys. J. C **11**, 111 (1999)
24. M. Hansson, H. Jung, arXiv:hep-ph/0309009
25. A. Edin, G. Ingelman, J. Rathsman, Phys. Lett. B **366**, 371 (1996). arXiv:hep-ph/9508386
26. A. Edin, G. Ingelman, J. Rathsman, Z. Phys. C **75**, 57 (1997). arXiv:hep-ph/9605281
27. J. Rathsman, Phys. Lett. B **452**, 364 (1999). arXiv:hep-ph/9812423
28. A. Edin, G. Ingelman, J. Rathsman, Comput. Phys. Commun. **101**, 108 (1997). arXiv:hep-ph/9605286
29. M. Bengtsson, T. Sjöstrand, Z. Phys. C **37**, 465 (1988)
30. M. Bengtsson, G. Ingelman, T. Sjöstrand, in *Proc. of the HERA Workshop 1987*, vol. 1, ed. by R.D. Peccei (DESY, Hamburg, 1988), p. 149
31. J. Pumplin et al. J. High Energy Phys. **0207**, 012 (2002). arXiv:hep-ph/0201195
32. B. Andersson, G. Gustafson, G. Ingelman, T. Sjöstrand, Phys. Rep. **97**, 31 (1983)
33. T. Sjöstrand, Comput. Phys. Commun. **135**, 74 (2001)
34. T. Sjöstrand, S. Mrenna, P. Skands, J. High Energy Phys. **0605**, 026 (2006). arXiv:hep-ph/0603175
35. Z. Nagy, Z. Trocsanyi, Phys. Rev. Lett. **85**, 082001 (2001). arXiv:hep-ph/0104315
36. W.J. Marciano, Phys. Rev. D **29**, 580 (1984)
37. S. Bethke, Eur. Phys. J. C **64**, 689 (2009). arXiv:0908.1135 [hep-ph]
38. L. Lönnblad, Comput. Phys. Commun. **71**, 15 (1992)
39. I. Abt et al. (H1 Collaboration), Nucl. Instrum. Methods Phys. Res. A **386**, 310 (1997)
40. I. Abt et al. (H1 Collaboration), Nucl. Instrum. Methods Phys. Res. A **386**, 348 (1997)
41. R. Appuhn et al. (H1 SPACAL Group), Nucl. Instrum. Methods Phys. Res. A **386**, 397 (1997)
42. B. Andrieu et al. (H1 Calorimeter Group), Nucl. Instrum. Methods Phys. Res. A **336**, 499 (1993)
43. B. Andrieu et al. (H1 Calorimeter Group), Nucl. Instrum. Methods Phys. Res. A **350**, 57 (1994)
44. M. Peez, Ph.D. thesis, DESY-THESIS-2003-023, University of Lyon, 2003, available from http://afs/desy.de/group/h1/psfiles/theses/h1th-317.ps
45. P. Van Esch et al. Nucl. Instrum. Methods Phys. Res. A **446**, 409 (2000). arXiv:hep-ex/0001046
46. S. Bentvelsen et al., in *Proceedings of the Workshop "Physics at HERA"*, ed. by W. Buchmüller, G. Ingelman (DESY, Hamburg, 1992), p. 23
47. C. Hoeger et al., in *Proceedings of the Workshop "Physics at HERA"*, ed. by W. Buchmüller, G. Ingelman (DESY, Hamburg, 1992), p. 43
48. A. Glazov, N. Raicevic, A. Zhokin, Comput. Phys. Commun. **181**, 1008 (2010)
49. S. Catani, Y. Dokshitzer, B. Weber, Phys. Lett. B **285**, 291 (1992)
50. M. Cacciari, G.P. Salam, G. Soyez, Phys. Lett. B **641** (2006). arXiv:hep-ph/0512210
51. R. Brun, R. Hagelberg, M. Hansroul, J.C. Lassalle, CERN-DD-78-2-REV
52. A. Kwiatkowski, H. Spiesberger, H.J. Möhring, Comput. Phys. Commun. **69**, 155 (1992)
53. R. Polifka, Ph.D. thesis, DESY-THESIS-2011-025, Charles University in Prague, 2011, available from http://afs/desy.de/group/h1/psfiles/theses/h1th-655.pdf
54. V. Blobel, arXiv:hep-ex/0208022
55. F.D. Aaron et al. (H1 Collaboration), Eur. Phys. J. C **66**, 17 (2010). arXiv:0910.5631
56. K. Nowak, Ph.D. thesis, DESY-THESIS-2010-011, University of Zürich, 2009, available from http://www-h1.desy.de/psfiles/theses/h1th-520.pdf
57. D. Salek, Ph.D. thesis, Charles University in Prague, 2010, available from http://www-h1.desy.de/psfiles/theses/h1th-617.pdf
58. E. Kuraev, L. Lipatov, V. Fadin, Sov. Phys. JETP **44**, 443 (1976)
59. E. Kuraev, L. Lipatov, V. Fadin, Sov. Phys. JETP **45**, 199 (1977)
60. I. Balitsky, L. Lipatov, Sov. J. Nucl. Phys. **28**, 822 (1978)